INTERFEROMETRIC SYNTHETIC APERTURE RADAR (INSAR) FOR FINE-RESOLUTION BASAL ICE SHEET IMAGING

BY

William Arthur Blake

Submitted to the graduate degree program in Electrical Engineering
and the Graduate Faculty of the University of Kansas
in partial fulfillment of the requirements for the degree of
Doctor of Philosophy.

_____
Chairperson

Committee member _____

_____

_____

_____

Date defended: _____

The Dissertation Committee for William Arthur Blake certifies that this is the approved version of the following dissertation:

INTERFEROMETRIC SYNTHETIC APERTURE RADAR (INSAR) FOR FINE-RESOLUTION BASAL ICE SHEET IMAGING

_____
Chairperson *

Date approved: _____

To my loving wife Sheena, daughter Kiersten, Mom, and Dad

Acknowledgments

Just like it takes a community to raise a child, any great accomplishment is not the result of one person. There are many people that I would like to thank for their support and help through my graduate career.

My family has been essential to my success. My wife Sheena for putting up with the long hours I have put in and my traveling the world to conferences and field work, some within weeks of the birth of our first child. She has been so supportive at every step, twist, and turn. Mom for giving me her advice and wisdom over the years, and Dad for my sense of humor and strong will, who I sincerely miss and wish you were able to be here for this accomplishment.

I would like to thank my adviser Dr. Allen for his constant motivation and advice. Just 5 years ago I took “Intro to Radar” from him and haven't looked back since. All those that I have had “working” lunches with over the years: Lei Shi, Cameron Lewis, Chris Prokopiak, and Victor Jara who rekindled my love of flying. My office-mate and occasional golf partner Ben Panzer, for working through derivations and keeping me sane. Logan Smith and Anthony Hoch for their work with me on the signal processing team and the CSARP project, truly great colleagues and friends. There are many others that have helped me through the years, but too many to list; to all those I am also grateful.

I would also like to recognize NSF grant ANT-0424589 for the support of CReSIS and myself and NASA grant NNX07A039H for their earth and space science fellowship.

Table of Contents

Figure Index

Table Index

Equation Index

1 Background and Literature Review

1.1 Motivation

Understanding the response of ice sheets to future climate change is of major concern. Section 8.2.1 of the IPCC report released in 2007 states that the “Limited knowledge of ice sheet and ice shelf processes leads to unquantified uncertainties in projections of future ice sheet mass balance, leading in turn to uncertainty in sea-level rise projections” [IPCC 2007]. To model the component of sea level rise related to the ice's response to global climate change several key factors related to mass balance are needed. Accurate knowledge of both the basal topography and composition is very important to refining these models. A big drawback to the IPCC report is the large margin of error in the ice sheets' response to climate change. The Scientific Committee on Antarctic Research (SCAR) explained the need for more realistic ice-sheet models in a report by Van der Veen and others in 2007. More realistic models require basal measurements with spacings of “no more than a few hundred meters”, with more samples being preferred over key areas.

Two of the most common techniques used for mapping basal topography are seismic and radar depth sounding. Previous measurements of 3-D ice sheet topography and composition have been conducted by seismic measurements with sample spacing on the order of kilometers. A radar depth sounder works well if you can meet the cross track spacing requirements, which typically requires many more flights than is feasible for a survey in terms of both time and money. Additionally, there are inherent angle-of-arrival ambiguities that cannot be resolved with

basic nadir-looking beam formation. Using a depth sounder radar with interferometric processing allows us to produce a finer resolution topographic survey with many fewer passes; instead of only collecting a line of data you are able to collect a swath and resolve angle-of-arrival ambiguities. This will enable more realistic ice sheet models, as desired by the SCAR report. With the angle of arrival resolved, backscatter maps versus angle of arrival can be created and conclusions can be drawn on the basal composition, which in turn helps to refine ice sheet models. Thus I propose to develop interferometric synthetic aperture radar (InSAR) algorithms appropriate for the ice depth sounding application and use this technique to create a basal topography and reflectivity maps.

1.2 Literature Review

The first principle involved with InSAR processing is interferometry. Interferometry refers to a method in which the phase difference between two signals is used to provide better insight to how those signals are related to each other. Interferometry provides the ability to use two observations to know the position of a target more accurately than is possible with just one observation. However by itself it cannot resolve range ambiguities. Therefore, you have subwavelength position accuracy but also range ambiguities.

Another aspect of InSAR is synthetic aperture radar (SAR) processing. SAR creates a synthetic antenna using multiple samples of a scene collected from different locations. Usually these multiple samples are taken from a moving platform over a stationary target. SAR processing provides fine along-track resolution; however, in typical SAR applications, only the

magnitude of the signal is preserved while the signal phase is discarded.

InSAR combines interferometry with SAR, as the name implies. InSAR utilizes two complex SAR images produced from samples collected at different measurement positions and registered to look at identical locations. With these two registered images, a comparison of phase information can be calculated on a pixel-by-pixel basis and used to directly determine height information. First reported in 1974, Graham used an airborne radar with two vertically separated antennas to generate an interferogram. Graham simply added the analog signals from the two antenna locations to generate an image with nulls where the signals canceled. By combining the spacings between the nulls with range data, Graham determined the topography of the terrain below. However, he concluded that since the nulls where ambiguous, a reference height in the scene was necessary to calibrate the interferogram.

In 1990 Li and Goldstein formed a simple, direct relationship between phase difference and height. Their main goal was to develop a relationship for the estimation of height errors from phase for different spaceborne baselines and signal-to-noise ratios. This relationship, although developed specifically for spaceborne applications, can be derived for other platforms and baselines as well. Heights related to phase are relative heights and therefore require a target of known height in the scene.

InSAR is well-established as an excellent tool for surface topography mapping [Zebker and Goldstein 1986]. However, it has also been used to give insight into things like forest coverage and tree height. InSAR data analysis to give insight into forested terrain was first done by Hagberg, Ulander, and Askne in 1995. They used repeat passes of ERS-1 data and showed

that tree height could be estimated relative to an open field and verified their estimates with in situ measurements. Further work was done on the use of InSAR for forestation coverage as well as L and C band comparisons by Yong et al. 2003. In 2008, using a similar technique Zhoung et al. used InSAR to map water level changes in a swamp forest using ERS and RadarSat-1 data. Zhoung used the principle of double bounce off trees/vegetation trunks and the water below it to maintain coherence across an image. Using this technique, the relative water levels could be estimated. Additionally, Treuhaft et al. in 1996 used multibaseline InSAR to estimate vegetation depth. They used the known topography compared with the InSAR generated topography to determine the vegetation height.

The majority of work using InSAR on the cryposphere has been focused on measurements of the surface topography and velocity [Forster, Jezek, et al. 1998][Weber Hoen and Zebker 2000][Yamanokuchi et al. 2006]. However there are several instruments capable of performing depth sounding on the ice sheets. These are the P-sounder by the Technical University of Denmark [Dall et al. 2007], a Terrestrial and Planetary Imaging Radar (TAPIR) an HF sounder [Le Gall et al. 2008], and a depth sounder developed by the British Antarctic survey (BAS) [Heliere et al. 2007]. These radars are either not capable of, have not been able to, or have not attempted to perform InSAR processing on their data.

Performing InSAR processing for sub-glacial bed mapping using depth sounding presents unique challenges. First, there has been no work done using InSAR through a deep medium without a known topography. Additionally, there are no known calibration targets at the base of the ice, so the relative heights provided by InSAR will need to be calibrated without an explicit

calibration target. Some researchers have looked at performing InSAR through the ice sheets, including the Global Ice Sheet Mapping Orbiter (GISMO) [Jezek et al. 2006-1]. No results have yet been published on these results, although a lot of proof-of-concept work has been done [Jezek et al. 2006-2].

Another technique to form basal images from multi-aperture depth sounder data is tomography, which uses a technique like multiple signal classification (MUSIC). The MUSIC algorithm requires more looks than desired signals (in this case there are two desired signals, one from the left and another from the right, and 8 looks from the receivers). MUSIC is typically used for direction of arrival estimation and selects the largest eigenvalues. MUSIC performs well in high SNR areas; however, like InSAR, after MUSIC is applied reflectivity measurements are lost, since the magnitudes of the values after the MUSIC algorithm is applied are no longer relative to other records. InSAR is not a parametric approach and can theoretically be used in lower SNR areas, but it is susceptible to layover and shadowing. The MUSIC algorithm does provide another interesting option for 3-D basal imaging and most likely future work [Paden et al 2010].

2 InSAR Overview and Derivation

2.1 InSAR Introduction

InSAR uses two observations of a scene to determine the height of a target above a reference plane. The observation geometry in relationship to the target is shown in figure 2.1. Sections 2.1-2.4 of this document will go through the derivation of equations for InSAR. Section 2.5 relates the equations to the specific geometry for basal ice imaging.

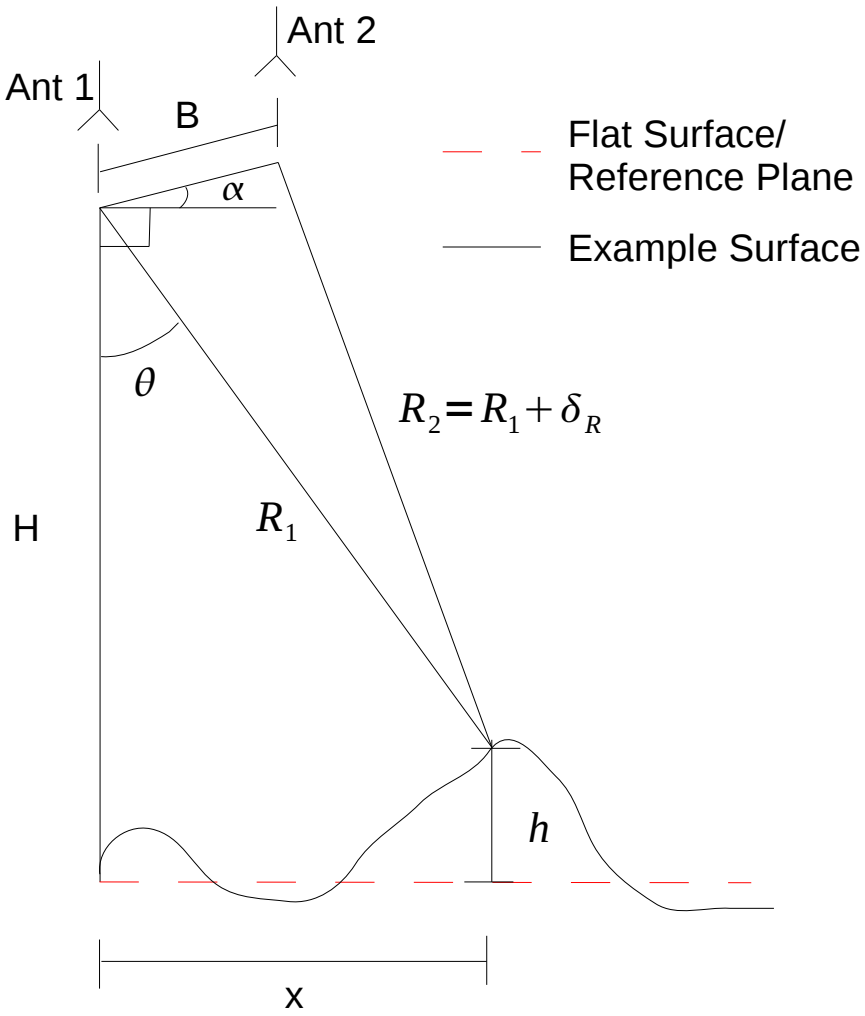

Figure 2.1: InSAR geometry

Where R_1 and R_2 are ranges to the target. H is the height of antenna element 1 over a reference plane, x is the cross track distance to a target, θ is the look angle, α is the angle between antenna elements 1 and 2 relative to the horizon, B is the baseline distance between antenna 1 and 2 and h is the height of the target relative to the reference plane.

Looking at the equations for R_1 and R_2 we have:

$$R_2 = R_1 + \delta_R$$

$$R_1 = \sqrt{(H-h)^2 + x^2}$$

$$R_2 = \sqrt{(H - h + B\sin(\alpha))^2 + (x - B\cos(\alpha))^2}$$

The target signal phases are dependent on the operating mode (see section 2.2). Depending on which antenna we assign to transmit and which we assign to receive, the phase difference will change. The basic formulation is:

$$\Phi_1 = \frac{2\pi R_{TOT1}}{\lambda}$$

$$\Phi_2 = \frac{2\pi R_{TOT2}}{\lambda}$$

where R_{TOT1} and R_{TOT2} are the total distances from the transmitter to the target and back to the receivers.

Looking at the difference between the phase to the two targets δ_Φ we get:

$$\delta_\Phi = \Phi_1 - \Phi_2$$

$$\delta_\Phi = \left(\frac{2\pi R_{TOT1}}{\lambda}\right) - \left(\frac{\pi R_{TOT2}}{\lambda}\right)$$

$$\delta_\Phi = k\left(R_{TOT1} - R_{TOT2}\right)$$

where k is the wavenumber $k = \frac{2\pi}{\lambda}$

This simplifies to:

$$\delta_{\Phi} = a\, k\, \delta_R \tag{1}$$

or alternatively, solving for δ_R

$$\delta_R = \frac{\delta_{\Phi}}{a\, k} \tag{2}$$

where k is the wavenumber and a is a coefficient applied to δ_R based on the operating mode (defined in the following section); a is defined as:

$$a = \frac{R_{TOT1} - R_{TOT2}}{R_1 - R_2}$$

The coefficient a also multiples the baseline, B, to make it seem larger. The effect of the coefficient a on the baseline is derived in section 2.4.

2.2 InSAR Operating Mode

To determine the relationship between phases and ranges we have to look at what mode we are operating in. There are several typical modes, single pass, multi-pass, and ping-pong, shown graphically in figures 2.2 through 2.5 and described below.

2.2.1 Single-pass Mode (a = 1)

In single-pass mode, one antenna operates as a transmitter and both antennas act as unique receivers. In this mode the coefficient a is equal to 1 since both antennas share a common path from the transmitter to the target.

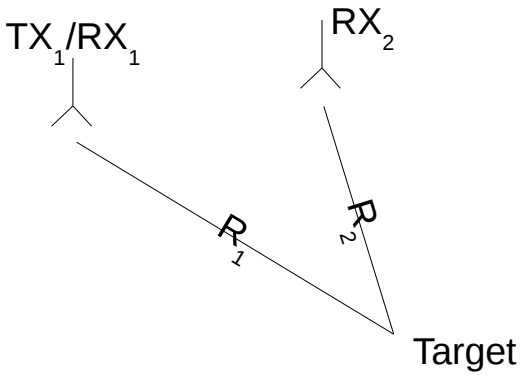

$$R_{TOT1} = R_1 + R_1$$

$$R_{TOT2} = R_1 + R_2$$

$$R_{TOT1} - R_{TOT2} = R_1 - R_2$$

$$a = (R_1 - R_2)/(R_1 - R_2)$$

$$= 1$$

Figure 2.2: Single-pass InSAR geometry

2.2.2 Multi-pass Mode (a = 2)

In multi-pass mode, the antennas act as separate and unique transmitters and receivers. In this mode, the coefficient a is 2, since both paths to and from the target differ.

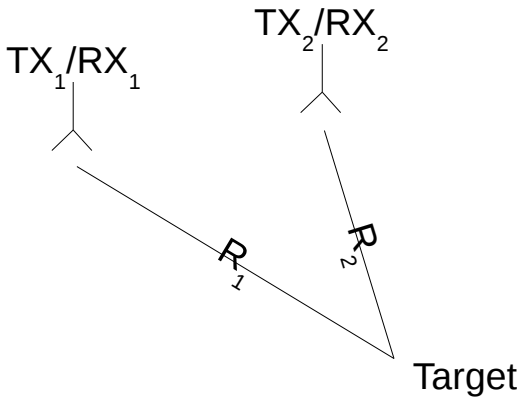

$$R_{TOT1} = R_1 + R_1$$

$$R_{TOT2} = R_2 + R_2$$

$$R_{TOT1} - R_{TOT2} = 2(R_1 - R_2)$$

$$a = 2(R_1 - R_2)/(R_1 - R_2)$$

$$= 2$$

Figure 2.3: Multi-pass mode geometry

2.2.3 Ping-pong Mode (a = 2)

Ping-pong refers to alternating transmitting on antennas 1 and 2 for each consecutive pulse. When antenna 1 is acting as a transmitter, it also receives that pulse. Likewise, when antenna 2 transmits it also receives. Mathematically it is identical to the multi-pass case. Ping-pong mode

provides the advantage of an increased baseline, since a is 2.

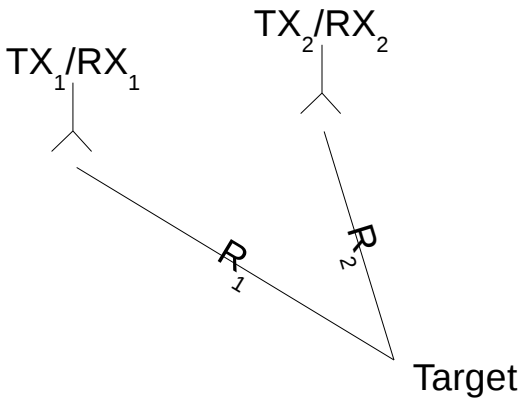

$$R_{TOT1} = R_1 + R_1$$

$$R_{TOT2} = R_2 + R_2$$

$$R_{TOT1} - R_{TOT2} = 2(R_1 - R_2)$$

$$a = 2(R_1 - R_2)/(R_1 - R_2)$$

$$= 2$$

Figure 2.4: Ping-pong mode geometry

2.2.4 Ping-pong with Common Receiver (a = 1)

in another implementation of ping-pong mode antennas 1 and 2 act as transmitters, alternating every other pulse, and both antennas share a common but separate receive antenna. In this case a would equal 1 since both paths share the common path from the target to RX_1. Operating in this mode does not provide the increased baseline, but only requires one receiver.

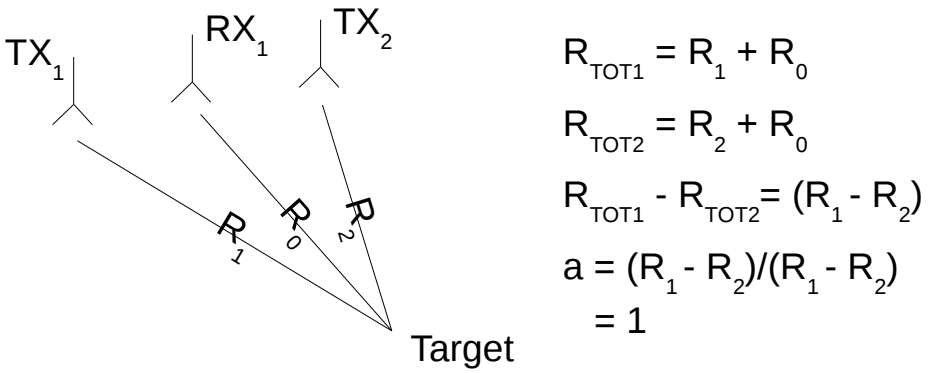

Figure 2.5: Ping-pong mode with common receiver geometry

2.3 InSAR δ_R Relationship

Next looking only at the geometry involving B, R_1, R_2, α, δ_R, and θ:

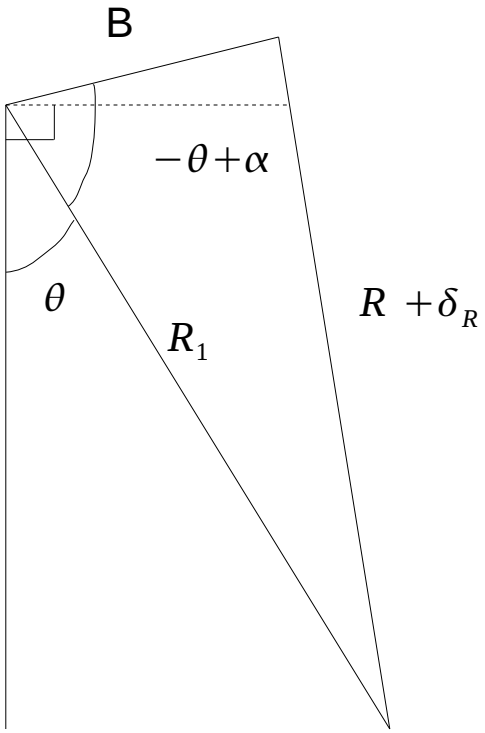

Figure 2.6: InSAR geometry for law of cosines relationship

Using the law of cosines:

$$(R_1+\delta_R)^2=R_1^2+B^2-2BR_1\cos(90-\theta+\alpha)$$

using $\cos(90-\theta+\alpha)=\sin(\theta-\alpha)$

$$R_1^2+2R\ \delta_R+\delta_R^2=R_1^2+B^2-\ BR_1\sin(\theta-\alpha)$$

$$R_1^2+2R_1\delta_R+\delta_R=R_1^2+B^2-BR_1\sin(\theta-\alpha)$$

$$2R_1\delta_R+\delta_R^2=B^2-2BR_1\sin(\theta-\alpha)$$

solving in terms of δ_R

$$\delta_R+\frac{\delta_R^2}{2R_1}=\frac{B^2}{2R_1}-\frac{2BR_1\sin(\theta-\alpha)}{2R_1}$$

$$\delta_R+\frac{\delta_R^2}{2R_1}=\frac{B^2}{2R_1}-B\sin(\theta-\alpha)$$

At this point normally you can simplify this equation if $2R_1 \gg B^2$ and $2R_1 \gg \delta_R^2$ which are typically valid assumptions, however they are not for our case causing up to 5% error.

Therefore we have to use:

$$\frac{\delta_R^2}{2R_1}+\delta_R=\frac{B^2}{2R_1}-B\sin(\theta-\alpha) \quad (3)$$

Combining equations 2 and 3 we get:

$$\frac{\delta_R^2}{2R_1}+\delta_R=\frac{B^2}{2R_1}-B\sin(\theta-\alpha) \quad (4)$$

Rearranging:

$$\delta_R^2 + 2R\delta_R - B^{\square} + 2R_1 B\sin(\theta-\alpha) =$$

Using the quadratic equation:

$$\delta_R = \frac{-2R_1 \pm \sqrt{4R_1^2 - 4(B^2 + 2R_1 B\sin(\theta-\alpha))}}{2}$$

$$\delta_R = -R_1 \pm \sqrt{R_{\square}^2 + B^2 - 2R_1 B\sin(\theta-\alpha)}$$

$$\delta_R = -R_1 + \sqrt{R_{\square}^2 + B^2 - 2R_1 B\sin(\theta-\alpha)} = \frac{\delta_{\Phi}}{ak}$$

Solving for θ we have:

$$-R_1 + \sqrt{R_1^2 + B^{\square} - 2R_1 B\sin(\theta-\alpha)} = \frac{\delta_{\Phi}}{ak}$$

$$\sqrt{R_1^2 + B^{\square} - 2R_1 B\sin(\theta-\alpha)} = \frac{\delta_{\Phi}}{ak} + R_{\square}$$

$$R_1^2 + B^{\square} - 2R_1 B\sin(\theta-\alpha) = \left(\frac{\delta_{\Phi}}{ak} + R_1\right)^2$$

$$\sin(\theta-\alpha) = \frac{-\left(\frac{\delta_{\Phi}}{ak} + R_1\right)^2 + R_1^2 + B^2}{2R_1 B}$$

$$\theta = \alpha + \sin^{-1}\left[\frac{-\left(\frac{\delta_{\Phi}}{ak} + R_1\right)^2 + R_1^2 + B^2}{2R_1 B}\right] \quad (5)$$

However to create a DEM it is necessary to find the height, either above or below the reference plane, of the target. This is defined as h in figure 2.1 and figure 2.7. The next section will derive the relationship between δ_R and h.

2.4 InSAR Height Calculation

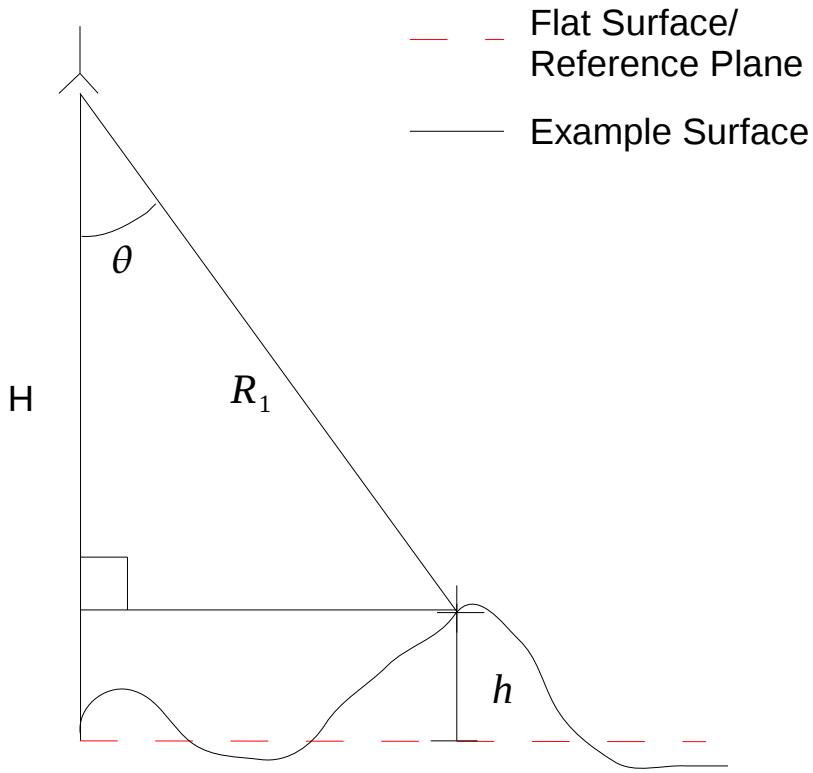

Figure 2.7: InSAR geometry for height calculation about a reference plane

Simplifying figure 2.1 to show just the relationship between R_1, h, θ and H we get figure 2.7. Looking at the cosine relationship of θ we have:

$$\cos(\theta)=\frac{H-h}{R_1}$$

solving for h

$$h=H-R_1\cos(\theta) \tag{6}$$

Therefore to determine h we need to know H, R_1, and θ.

Combining 5 and 6 we get:

$$h = H - R_1 \cos\left[\alpha + \sin^{-1}\left[\frac{-\left(\frac{\delta_\Phi}{a\,k} + R\right)^2 + R_1^2 + B}{R_1 B}\right]\right] \tag{7}$$

Now we have a formula only dependent on variables that are measurable, and a direct way to relate phase information to a height above/below a reference plane.

2.5 Specific NEEM InSAR Geometry

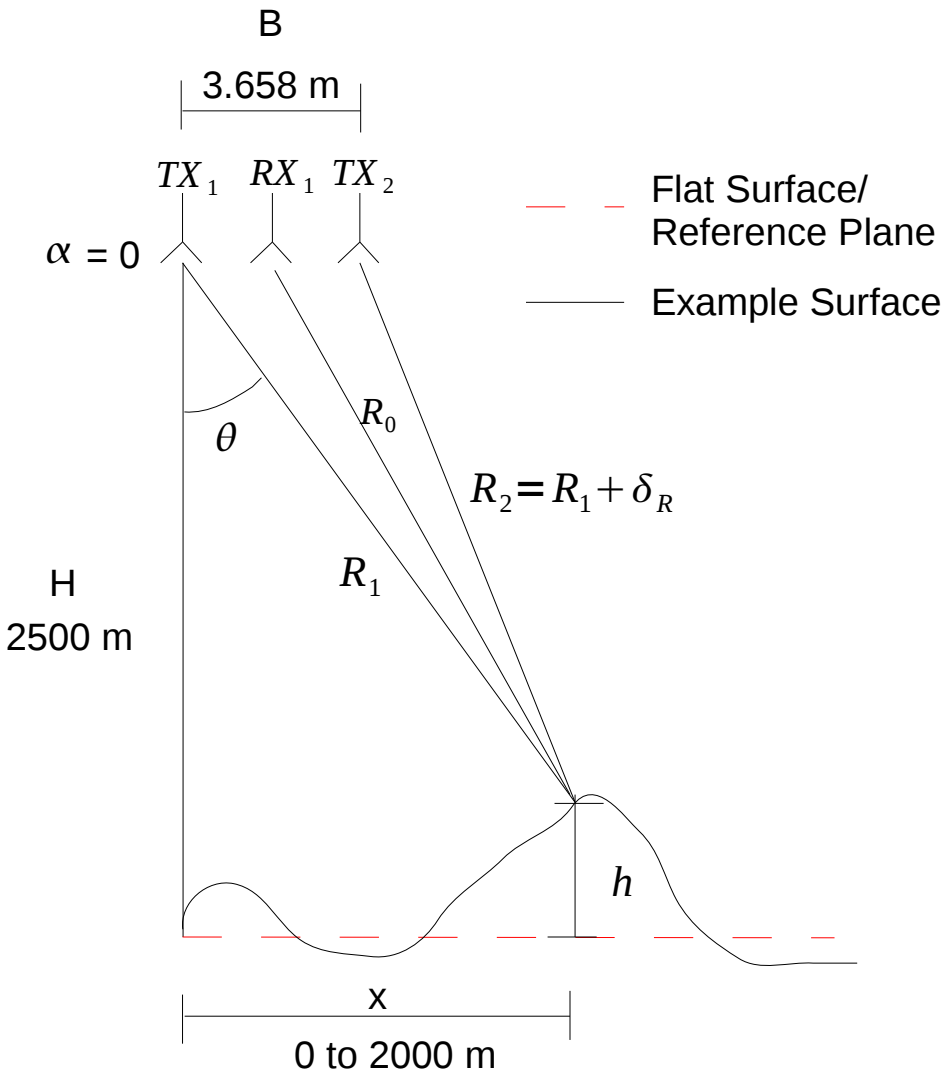

Figure 2.8: Specific NEEM InSAR geometry

The geometry for the ground-based InSAR system being used for this work has the values as shown in Figure 2.8. More discussion of the physical system is in section 3. The baseline between the transmitters B is 3.658 meters and the angle between them, α, is 0. The typical height of the antennas above the reference plane is 2500 m in ice. The x distances will vary

between 0 and 2000 m. For the data considered for this work there are two transmitters that share the same set of receivers (see figure 3.2). This was referred to as ping-pong mode with a common receiver during the derivation (section 2.2.4) therefore the a value for this case is 1. With this information we have everything necessary to perform InSAR processing.

3 NEEM Data Set

A ground-based radar survey was conducted by the Center for Remote Sensing of Ice Sheets (CReSIS) around the North Eemian (NEEM) drill site in Greenland, marked on figure 3.1. The NEEM project is an international collaboration headed by the Danes that started in 2007 and continues through 2011. The purpose of the NEEM project is to retrieve Eemian ice from the penultimate interglacial. These ice core samples will help us understand the dynamics of a past climate that would be similar to a future warming climate. Both airborne and ground-based radar surveys were conducted in 2007 to help identify the best area for the NEEM site. At that time the radar system did not detect the weakest deep internal layers due to hardware problems. An improved radar system was deployed in 2008 to image these deep layers. This system was capable of not only depth sounding but also supporting side-looking synthetic aperture radar imaging of the base of the ice.

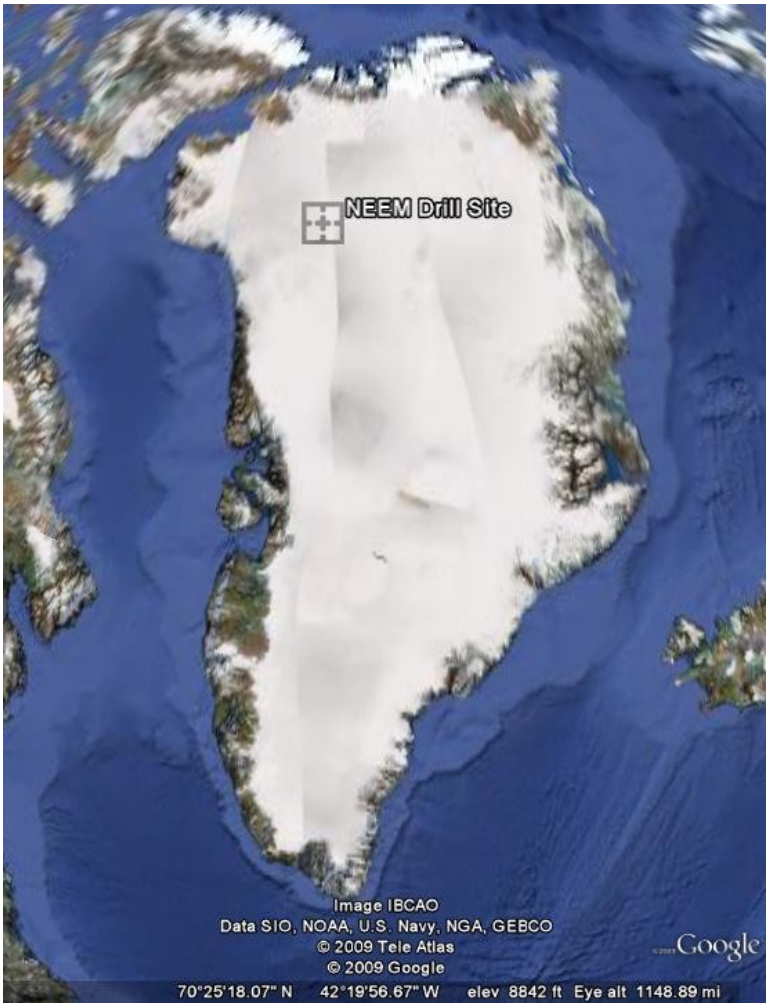

Figure 3.1: NEEM drill site in Greenland

3.1 Radar System Information

The multi-channel radar depth sounder (MCRDS) [Lohoefener 2006] system, as deployed for 2008, was a ground-based platform consisting of a single sled with four transmit antennas, two pairs forming two phase centers for left and right transmit. The transmitters were operated on alternating pulse repetition intervals (PRI) referred to as ping-pong mode. An overview of the system parameters can be seen in table 1.

Table 1: 2008 MCRDS System Parameters

Parameter	Value
Unique Transmitters	2
Unique Receivers	8
Center Frequency	150 MHz
Bandwidth	30 MHz
Pulse Duration	10 µs
Sampling Frequency	120 MHz
Range Resolution in Ice (after processing)	8 m
Azimuth Resolution in Ice (after processing)	4 m

The exact antenna spacings are shown in figure 3.2.

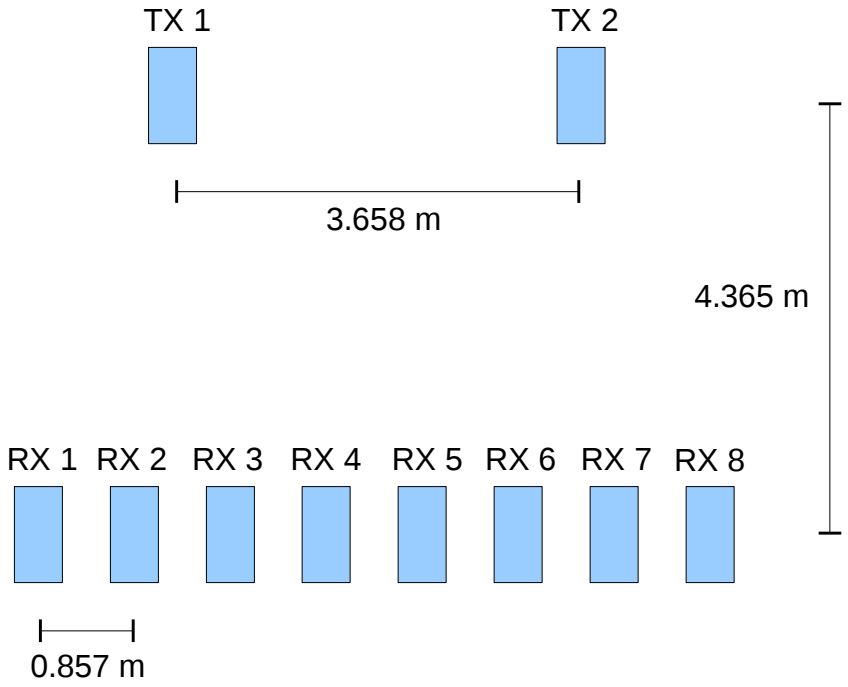

Figure 3.2: TX/RX antenna spacings

3.2 Survey Information

The NEEM drill site survey was conducted from August 7th to 16th of 2008. During the 8-day

survey just under 3 TB of data were recorded. There were 21 mostly east/west tracks, typically 10 km long, that were separated by 500 m, giving a total surveyed area of 100 km² centered on the drill site. Figure 3.3 shows the tracks where data were collected with regards to the drill site. The ice divide runs parallel to the northwest to southeast lines.

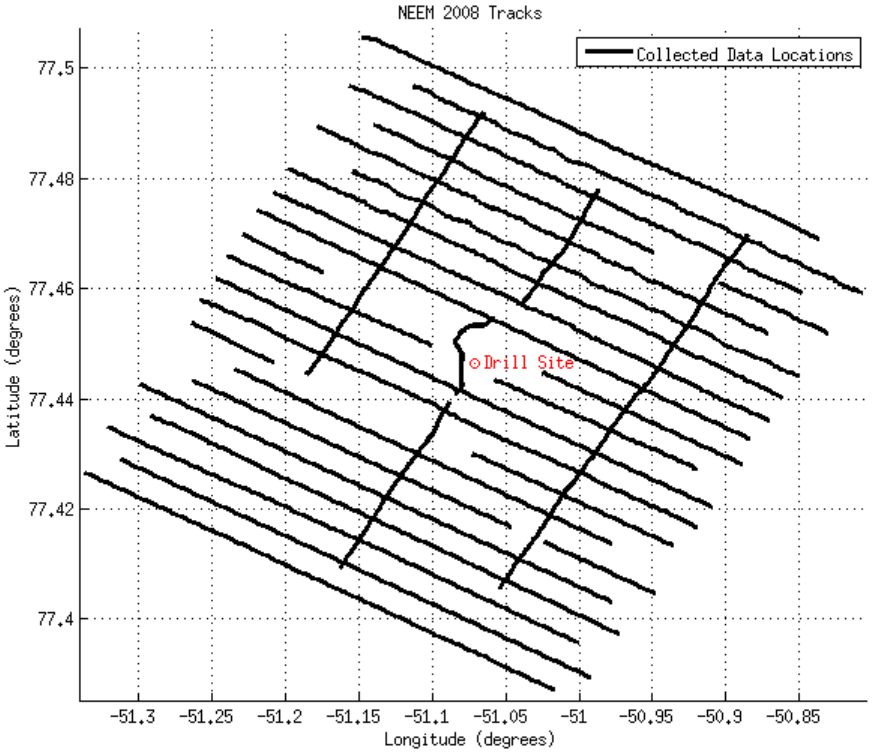

Figure 3.3: 2008 tracks around NEEM drill site

4 SAR and Preliminary InSAR Processing of NEEM Data

4.1 Processing Summary

A 2008 dataset from the NEEM drill site in Greenland will be the focus of the InSAR processing. These data have a very high SNR with a fairly strong off-nadir component. Data from each channel will undergo the following steps during processing (more explanation will given in the following sections):

1) Convert the data into a common file format called the CReSIS file format (CFF)

2) Linearly interpolate over the time "jumps" in header data to fix timing issues

3) Pulse compress with an ideal reference pulse and appropriate weighting to reduce range sidelobes

4) Bandpass filter, coherently integrate, and decimate the data in the range dimension to remove out of band interference and data volume

5) Coherent adaptive interference cancellation to remove 150 MHz interference spike

6) Removal of stopped records

7) Bandpass filter, coherently integrate, and decimate the data in the azimuth dimension to reduce data volume

8) SAR process the data using an f-k migration algorithm

9) Estimate bed depth from nadir focused echograms

10) Create coarse 3-D ice thickness map

11) Adaptively calibrate channels

12) Steer beam to +/- 20 degrees off nadir using all RX channels

13) Create side-looking SAR complex images

14) Perform coherence measurements between side-looking images

15) Fine-scale image registration

16) Create interferogram

17) Calculate interferometric phase

18) Height (DEM) calculation and estimate DEM errors

19) DEM accuracy verification

20) Overlay reflectivity

21) Scientific interpretation

A detailed analysis of each step is explained in the section 4.2.

4.2 Detailed Processing Description

4.2.1 Conversion Into the CReSIS File Format

Since the radar data are recorded in binary format, conversion to a standard format (CFF) was needed to be easily manipulated by MATLAB and processed. The CFF files have a very specific naming convention and structure set forth in the CSARP documentation [CSARP 2007]. In general the files are split into one channel of raw data per file with one file for header information and one file for position data. The position and the raw data files are in the HDF5 format with a .mat extension to save space and be readable on multiple platforms without the requirement of MATLAB. The header file is in ACSII and therefore human readable.

Figure 4.1 is an image generated from CFF data, showing an unprocessed echogram from

NEEM data collected on August 7th, 2008.

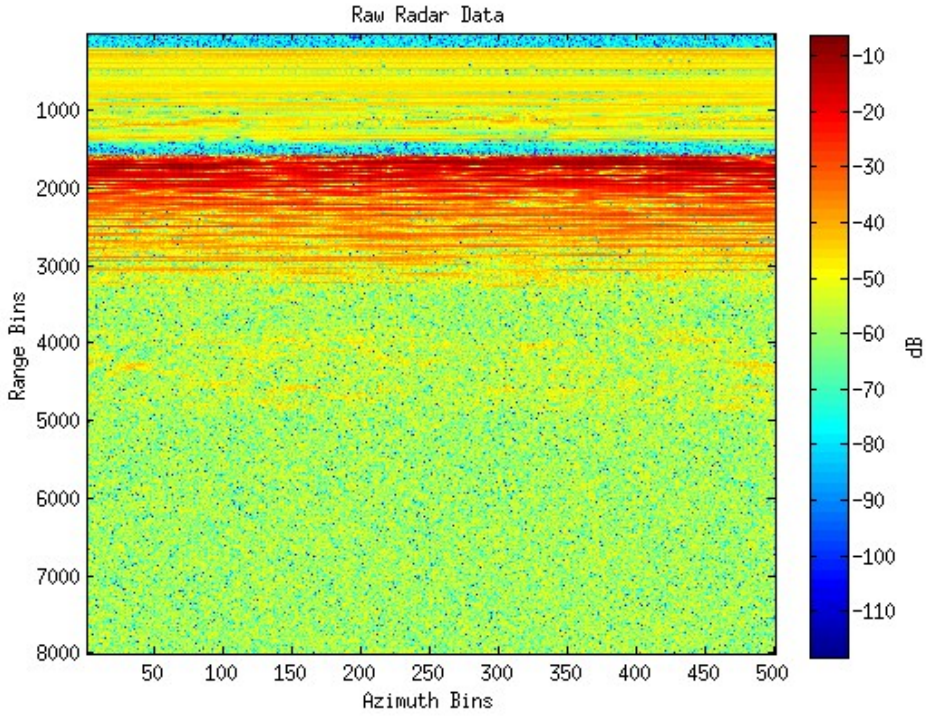

Figure 4.1: Plot of raw CFF formatted data

4.2.2 Fix Timing Issues with Linear Interpolation

During initial processing of the radar data there was an error with the computer and radar time stamps that caused these to "jump" forward about 10 secs and then a few minutes later jump back in time 10 secs. After further analysis of these time "jumps" it was apparent that they were artificially induced and could be corrected by matching the overall linear trend of the data and shifting the subset of data points that did not match that linear trend to fit with the rest. Therefore these artificial time jumps were corrected and removed.

4.2.3 Pulse Compression and Weighting to Reduce Range Sidelobes

The transmit pulse is a 10 µs waveform that chirps from 135 MHz to 165 MHz. The pulse has a 20 percent Tukey weighting on it, which combined with a double Blackman window can significantly reduce range sidelobes. It was necessary to reduce the range sidelobes as much as possible, since the bed return is very strong and one of the goals when creating the echograms is to see the deepest possible internal layers. This suppresses all range sidelobes by 80 dB, in theory, and at least 50 dB in practice. The penalties for this process are reduced signal to noise ratio and degraded resolution in the range dimension, both of which were acceptable trade-offs for these data.

The Tukey and Blackman weights used are shown in figures 4.2 and 4.3.

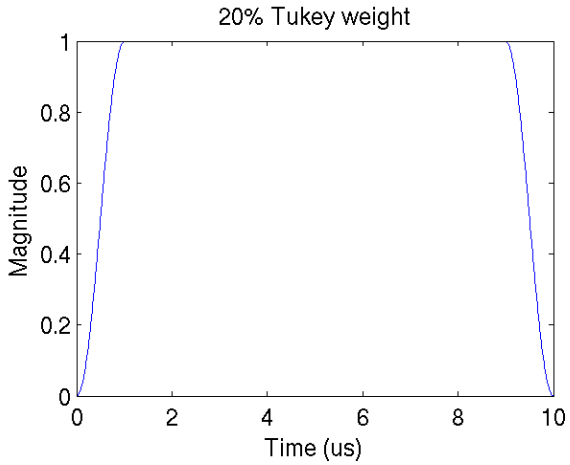

Figure 4.2: 20% Tukey weight

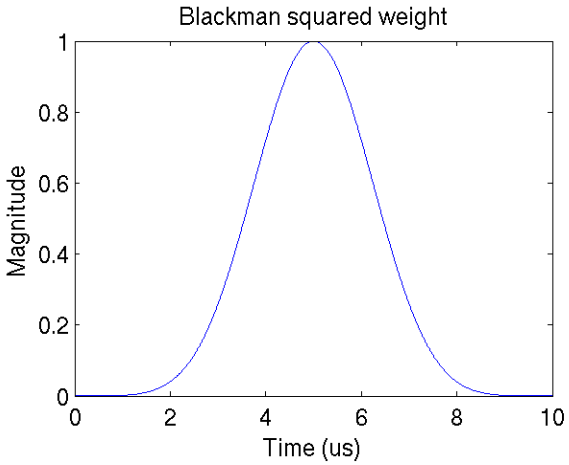

Figure 4.3: Blackman squared weight

Figure 4.4 shows the original unweighted chirp while figure 4.5 shows the chirp after weighting.

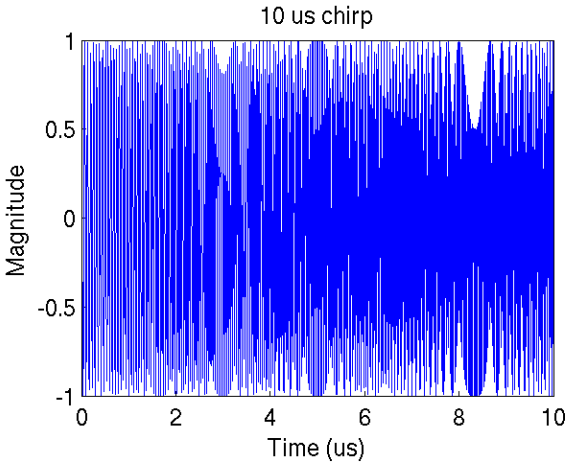

Figure 4.4: Unweighted reference chirp

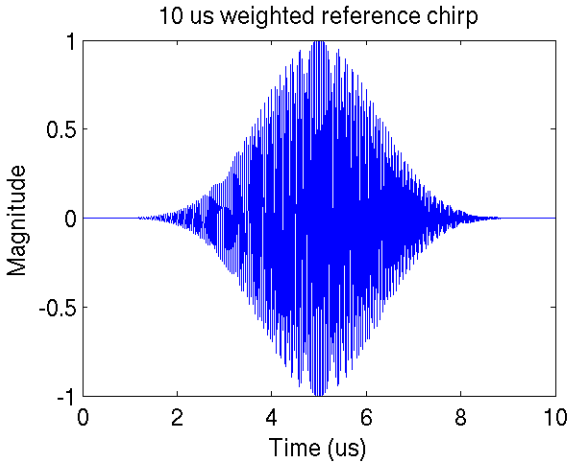

Figure 4.5: Weighted reference chirp

For verification of the sidelobe level the auto-correlation of the weighted reference chirp is shown in figure 4.6

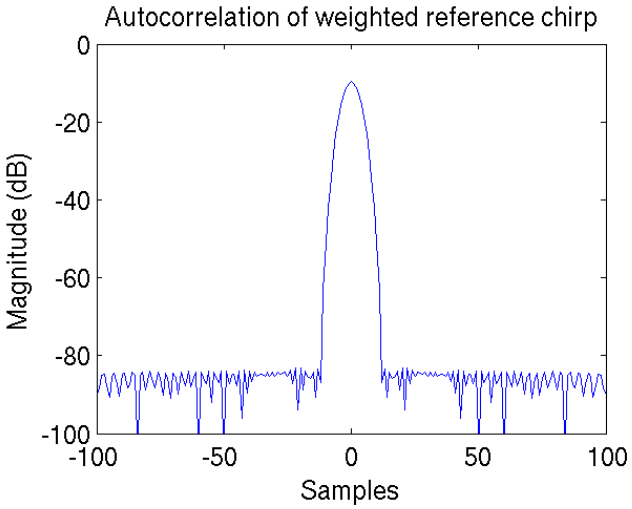

Figure 4.6: Autocorrelation of weighted reference chirp

The signal weighting is 0.42 for each Blackman and 0.88 for the Tukey, leading to a signal loss of 0.42*0.88*0.88 = 0.1552 = -8 dB. The resolution degradation is a factor of 1.68 for each Blackman and 1.01 for the Tukey, which works out to a increased resolution factor of

1.68*1.68*1.01 = 2.85. [Harris 1978] This causes our theoretical resolution for a 30 MHz bandwidth system to go from 2.8 m in ice to ~8 m in ice.

4.2.4 Filtering, Coherent Integration, and Decimation in Range

Next the data are filtered in the frequency domain to reduce the data volume and remove any out-of-band interference. The data were Tukey weighted in time with a 10 percent Tukey window then converted to the frequency domain and decimated to the band of interest (135 to 165 MHz) where they were converted back to the time domain. Doing this reduces the data volume by half, from 120 MHz real sampled data to 30 MHz I and Q sampled data.

Figure 4.7 is an image of the data after they have been pulse compressed, decimated, and filtered from the same August 7th data used in figure 4.1.

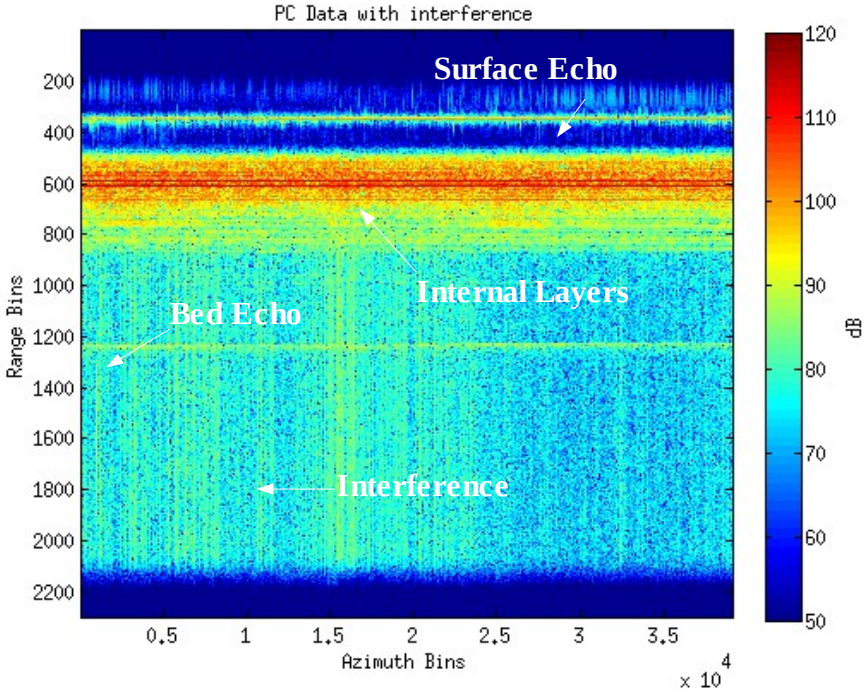

Figure 4.7: Pulse compressed data showing interference

As seen in figure 4.7 there are vertical interference streaks along the image that vary in intensity with time. Therefore further analysis of the interference and removal techniques was necessary.

4.2.5 Coherent Adaptive Interference Cancellation

The collected data have an interference signal that are spectrally concentrated at 150 MHz. The interference source was suspected to be leakage from a power supply. The amplitude and phase of the interference signal varied from record to record, but was constant within a record. The interference signal frequency was fairly constant at 150 MHz, but varied slightly. Therefore an adaptive interference cancellation algorithm was implemented that estimated the amplitude and phase of the largest peak in the frequency domain. If this peak was more than 3 dB larger than

the rest of the in-band frequencies then a signal with the amplitude equal to the interferer's and 180 degrees out of phase, was injected to remove the interference. This helped to preserve the desired data while removing the interference only when it was present.

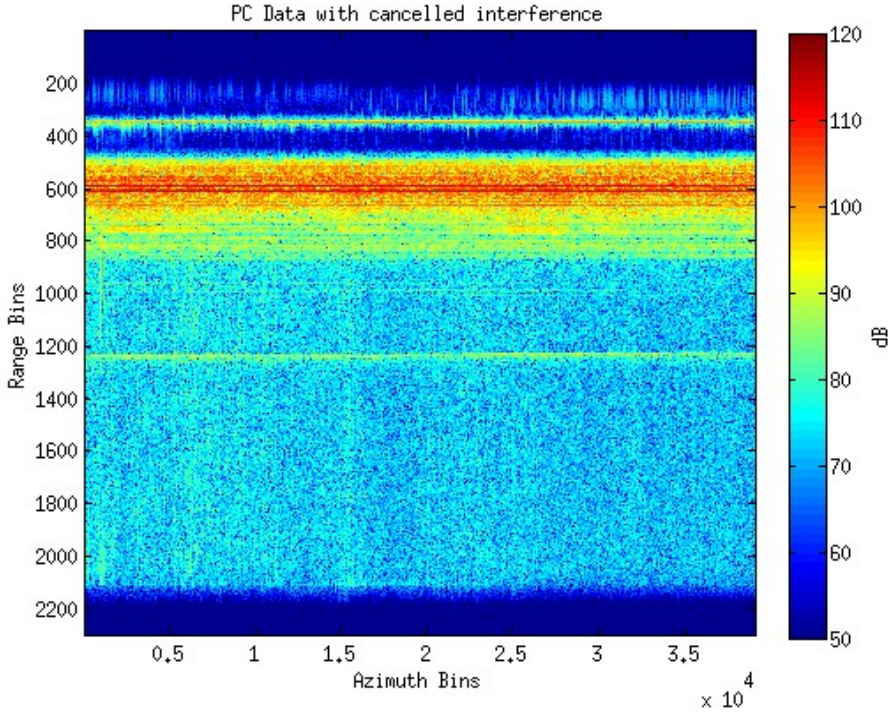

Figure 4.8: Pulse compressed data with interference removed

The interference is dramatically reduced (from 20 to 30 dB depending on the area) after adaptive noise removal.

4.2.6 Removal of Stopped Records

The ground-based platform stopped every couple of kilometers to collect data in a stationary mode. While useful for other science objectives these presented a hindrance for SAR processing using f-k migration which requires evenly spaced points. Hence the stationary data needed to be

detected and removed. To accomplish this the difference between GPS acquired locations was calculated and if the difference was too small (representing a stop) the corresponding data were removed. Although not perfect this was adequate for the f-k migration assumptions.

4.2.7 Filtering, Coherent Integration, and Decimation in Azimuth

A beamwidth of 10 degrees for SAR processing was selected due to slope effects and irregular platform motion. Since the data were oversampled in the slow time direction, to save both space and computational cost the data were decimated in the space-time domain to the 10 degrees of interest. A Hann weighting was applied to reduce sidelobes in the azimuth direction.

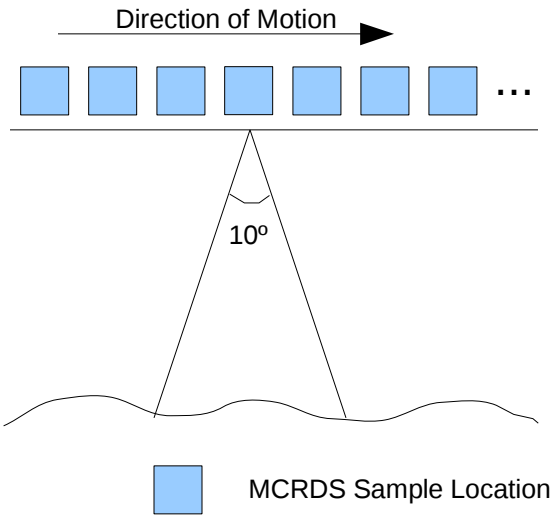

Figure 4.9: Graphical SAR processing representation

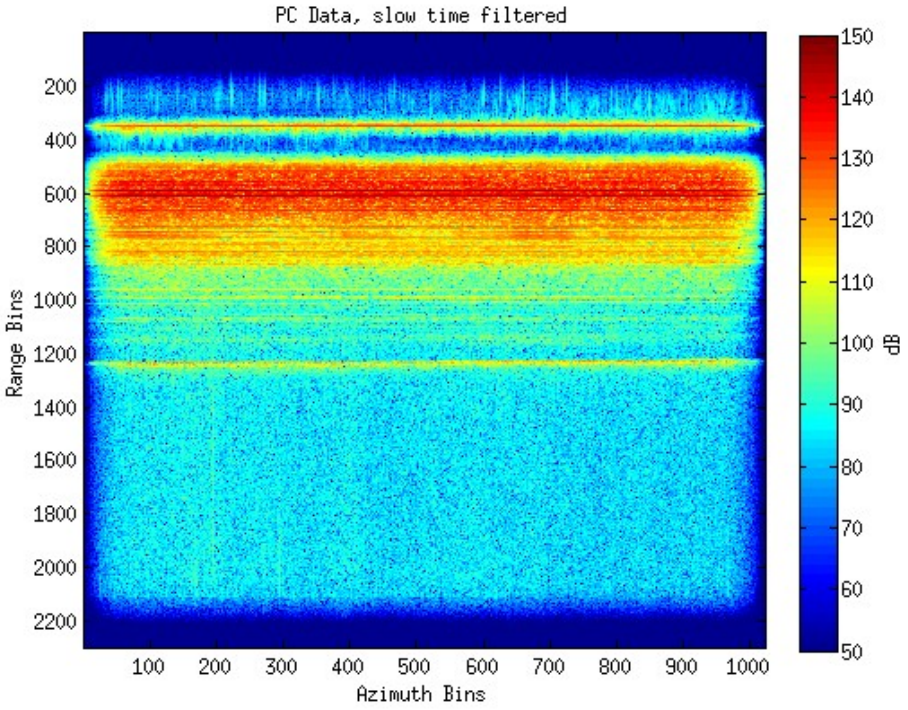

Figure 4.10: Pulse compressed data with azimuth filtering

A Tukey weighting is applied across the slow time direction before the 2-D FFT to reduce spectral spreading.

4.2.8 SAR Processing Using an F-k Migration Algorithm

Due to the fairly constant platform velocity an f-k migration algorithm was chosen to greatly improve the computation time versus a back projection time domain processor. The SAR processing algorithm has been verified to compress an ideal reference pulse with the appropriate SNR gain and resolution expected from this type of algorithm. The beamwidth used for the SAR processing was 10 degrees, leading to an azimuthal resolution of around 4 meters using the formula:

$$\Delta_R = \frac{\lambda R}{2L} \tag{8}$$

where Δ_R is the azimuth resolution, λ is the wavelength, R is the range to the target, and L is the length of the aperture. Using a nominal range of 2500 m, a wavelength of 1.12 m (150 MHz in ice), and a synthetic aperture length of 437 m (corresponding to a 10 degree beamwidth), we get:

$$\Delta_R = \frac{1.12 * 2500}{2 * 437} = 3.2\,m$$

Additionally there is a Hann window, to reduce spatial sidelobes, that increases the resolution by a factor of 1.2 making the resolution ~ 4 m.

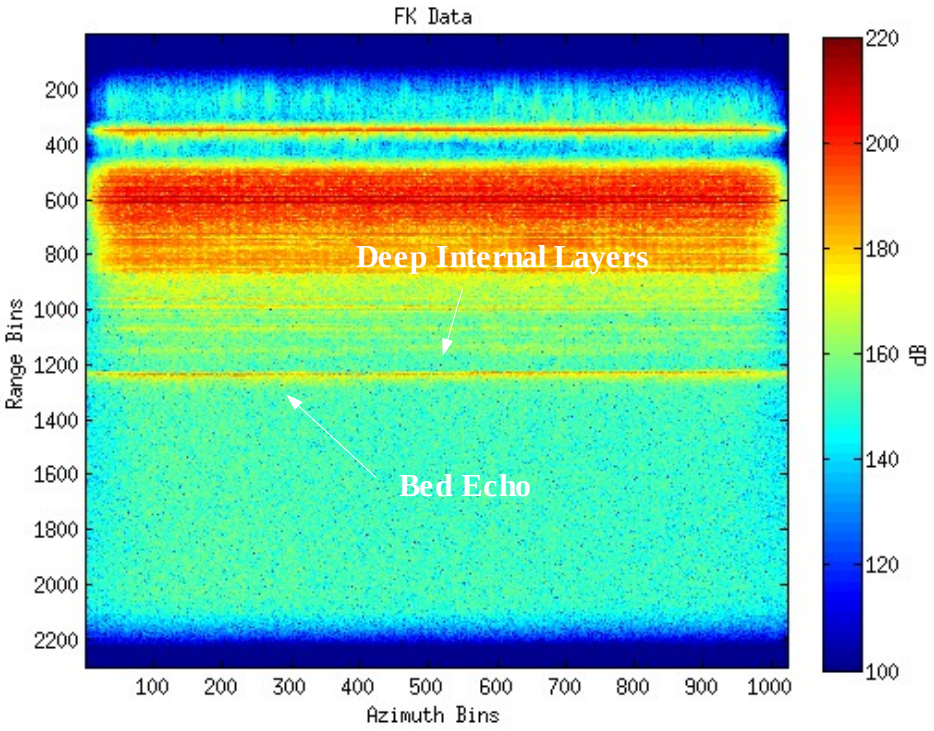

Figure 4.11: F-k migrated data

After f-k migration some of the deeper internal layering appears as seen in figure 4.11

4.2.9 Estimate Bed Depth

The large signal-to-noise ratio of the bed echo for these data combined with the fairly flat nature of the bed at NEEM made the bed estimation a pretty simple task. The largest return in the echogram over a user-selected section was chosen as the initial bed estimate. These data were then compared with a user selected noise section and (provided the SNR was large enough) the point was confidently chosen as the bed.

An example of the bed picking is shown in figures 4.12 and 4.13.

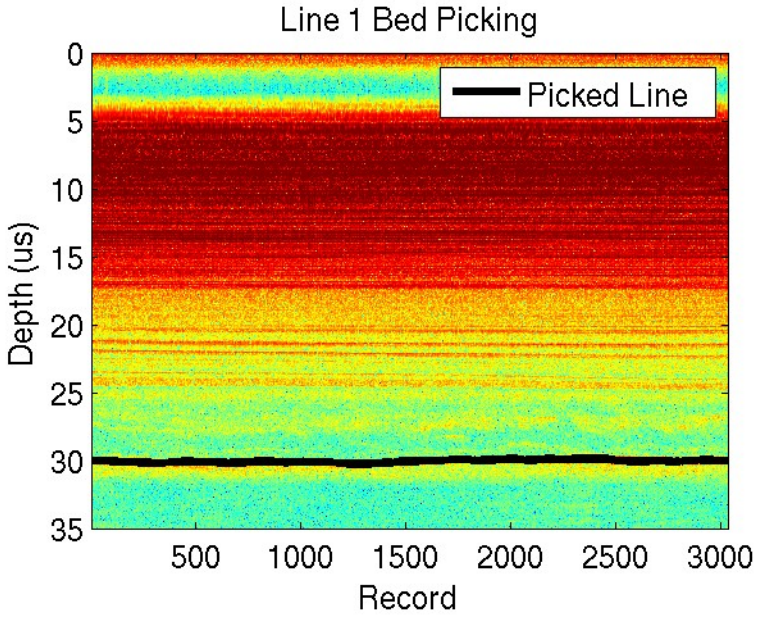

Figure 4.12: Line 1 bed picked

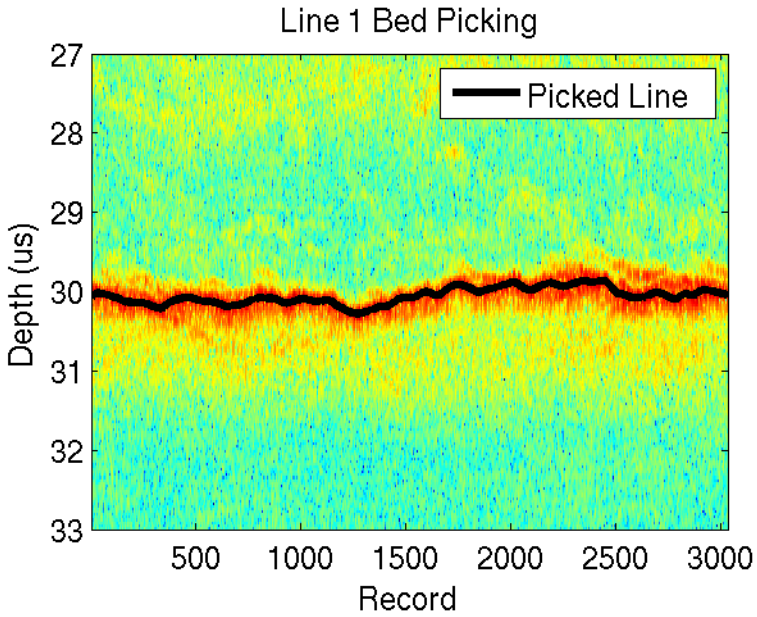

Figure 4.13: Line 1 bed picked zoomed

The automated picking method tracked the bed well across the entire image. At this point all bed depths are stored in terms of one way time. This allowed for any ice dielectric profile to

be used for exact depth calculations.

4.2.10 Create Coarse Resolution 3-D Bed Elevation Map

A coarse resolution 3-D basal digital elevation map (DEM) was created using the estimated bed locations combined with the appropriate latitude, longitude, and elevation. The estimated bed locations provides thickness information, and the GPS data provided surface elevation, with these two measurements an accurate DEM can be created. The coarse resolution DEM is shown in figure 4.14. Delaunay triangulation was used to interpolate between the 500 m spaced lines. Elevation is defined in terms of msl according to the WGS84 projection.

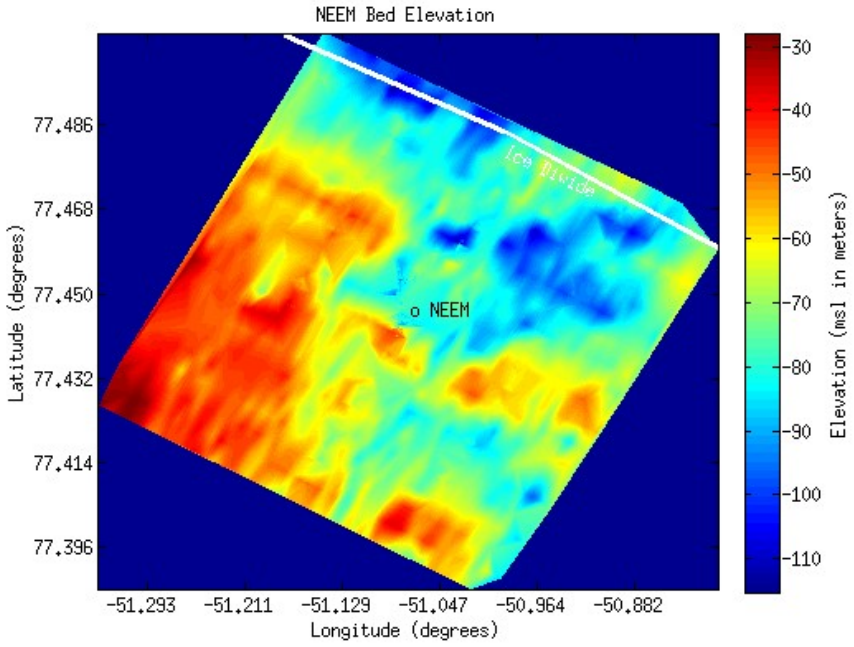

Figure 4.14: Coarse resolution DEM of NEEM data

4.2.11 Adaptively Calibrate Channels

Due to system imbalances in amplifiers and different lengths/characteristics of cables, and other components it is necessary to calculate complex coefficients to correct for both the amplitude and phase mismatch between channels. To do this a flat specular internal layer was selected as a calibration target. Signal data from the peaks in A-scope's from each of the individual channels (corresponding to the bed reflection) were analyzed in terms of their amplitude and phase. Amplitude and phase coefficients were calculated across an entire 10-km track resulting in a standard deviation of channel phase varied between 3.83 to 8.69 degrees. The calibration coefficients for the August 12th are shown in table 2 below.

Table 2: Calibration coefficients

Channel	Mean Phase (degrees)	Phase σ (degrees)	Mean Amplitude (volts)	Amplitude σ (volts)
1	0.00	0.00	1.00	0.00
2	-55.81	3.83	1.23	0.04
3	72.98	4.76	0.90	0.05
4	71.57	4.98	0.82	0.04
5	18.06	6.54	1.01	0.06
6	59.07	7.65	0.84	0.06
7	77.43	7.33	0.83	0.06
8	-4.45	8.69	0.86	0.07

As expected the standard deviation of the phase increases the further away from the reference channel you get. Overall the phases are well behaved across the day, but do vary slightly for each day therefore calibration coefficients were calculated for each day.

4.2.12 Steer Beam Off Nadir

To resolve left/right ambiguities the beam was digitally steered to +/- 15 degrees. Additionally to reduce the sidelobes, and therefore the return from the opposite side, a Hann weight was used. However a boxcar, Hann, Hamming and Blackman were all compared to determine the optimal weighting. Since the receive antenna spacing was 0.857 m this is less than $\frac{\lambda_{ice}}{2}$ for the ice medium. Where $\lambda_{ice} = \frac{v_p}{f_c}$ and $v_p = \frac{3e8}{\sqrt{3.15}}$. Making $\lambda_{ice} = 1.13\text{ m}$ and $\frac{\lambda_{ice}}{2} = 0.56\text{ m}$. Therefore grating lobes will start creeping in and if we attempt to steer the beam too far off nadir. However for the 7 – 22 degrees off nadir that we are steering the beam does not create a problem as the figures 4.15 through 4.18 show.

Our targets of interest are located from 300 m to 900 m off nadir, at a depth of 2500 m (in ice) this corresponds to angles of 7 degrees and 22 degrees respectively, so we want a beam pattern that preserves as much energy as we can toward the further off nadir targets as well as providing at least 30 dB of theoretical left/right isolation.

Looking at the following beam patterns a Hann weight was chosen because it preserved the most energy at 20 degrees while providing the desired isolation. A Blackman weighting could also have been used but there was an additional SNR loss of around 3 dB and the increased isolation was determined to not be necessary.

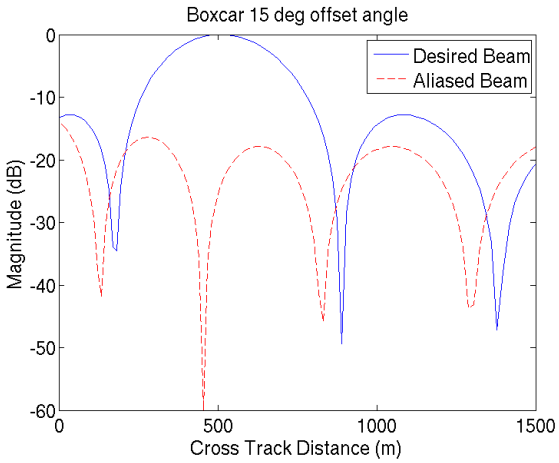

Figure 4.15: Boxcar steered array factor

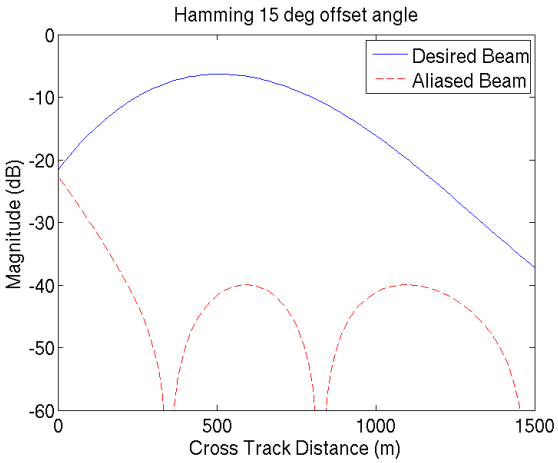

Figure 4.16: Hamming steered array factor

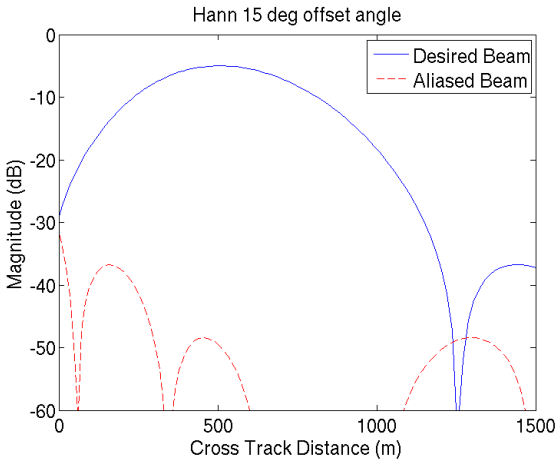

Figure 4.17: Hann steered array factor

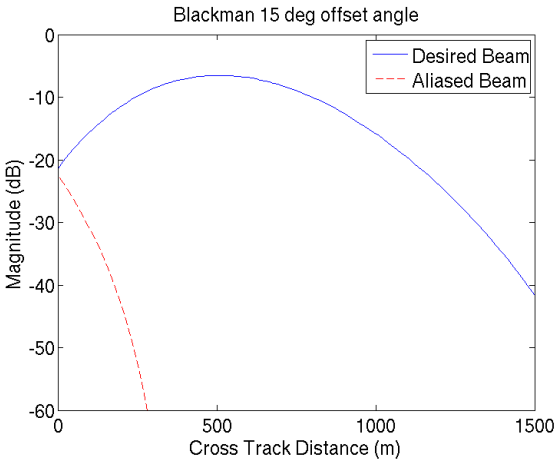

Figure 4.18: Blackman steered array factor

To verify that the correct angle was chosen the power of the beam steered to various off nadir angles are plotted in figures 4.19 through 4.22.

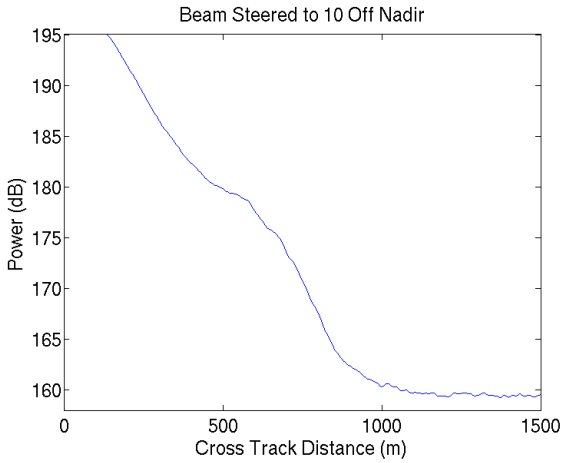

Figure 4.19: 10 degree steered beam power

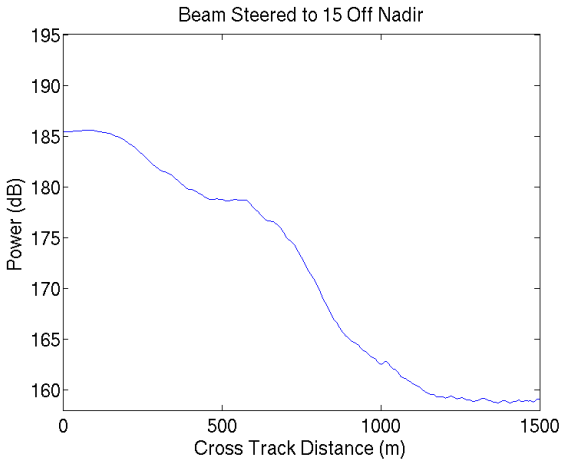

Figure 4.20: 15 degree steered beam power

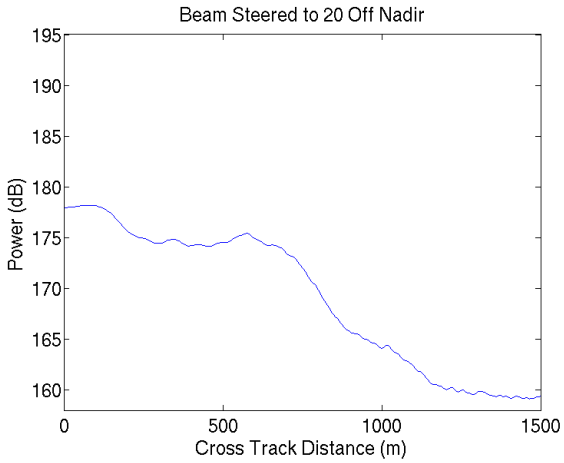

Figure 4.21: 20 degree steered beam power

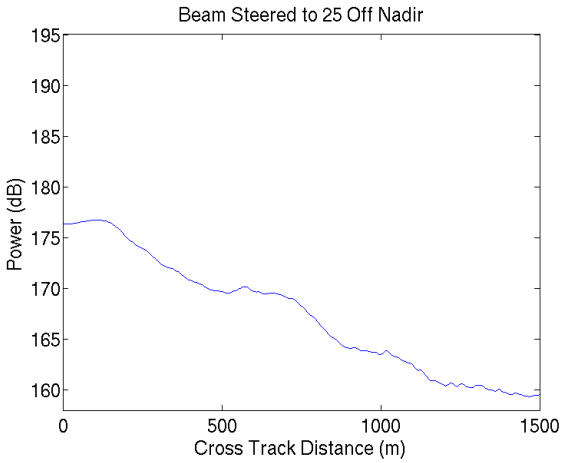

Figure 4.22: 25 degree steered beam power

The optimum weights and direction were determined to be Hann amplitude weights steered to +/- 15 degrees off-nadir. This preserved the most SNR for the off-nadir targets while suppressing the nadir returns as much as possible. Therefore these weights were used to combine the channels and create echograms that are steered to +/-15 degrees off-nadir.

4.2.13 Side-Looking SAR Complex Image Generation

To create a side-looking SAR image the beam steered data were projected to various cross-track

distances. Calculations where done to take into account how the firm refracts the signal through the ice in order to accurately project the data. The same technique that was used in [Paden 2006] was used for this compensation. The GISP ice core data were used to create a firn refraction profile. Then from this profile a look-up table of off-nadir distances versus time was created.

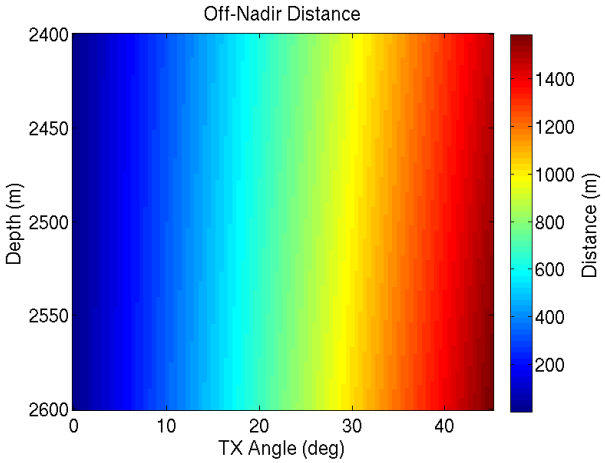

Figure 4.23: Cross-track distance without firn correction

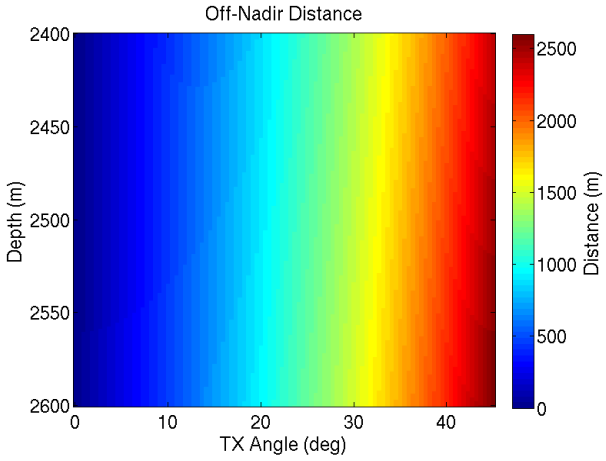

Figure 4.24: Cross-track distance with firn correction

Figure 4.23 shows the distance off nadir calculated from the transmission angle and the depth with the firn taken into account. Figure 4.24 shows the distance off nadir without the firn taken into account. For the angle of most interest, 7 – 22 degrees, the effect can be as much as a 50% over estimate in cross track distance.

Once the appropriate distances were calculated for the off nadir projection, the power could be reprojected onto the side-looking plane.

The initial side looking images look like the one below.

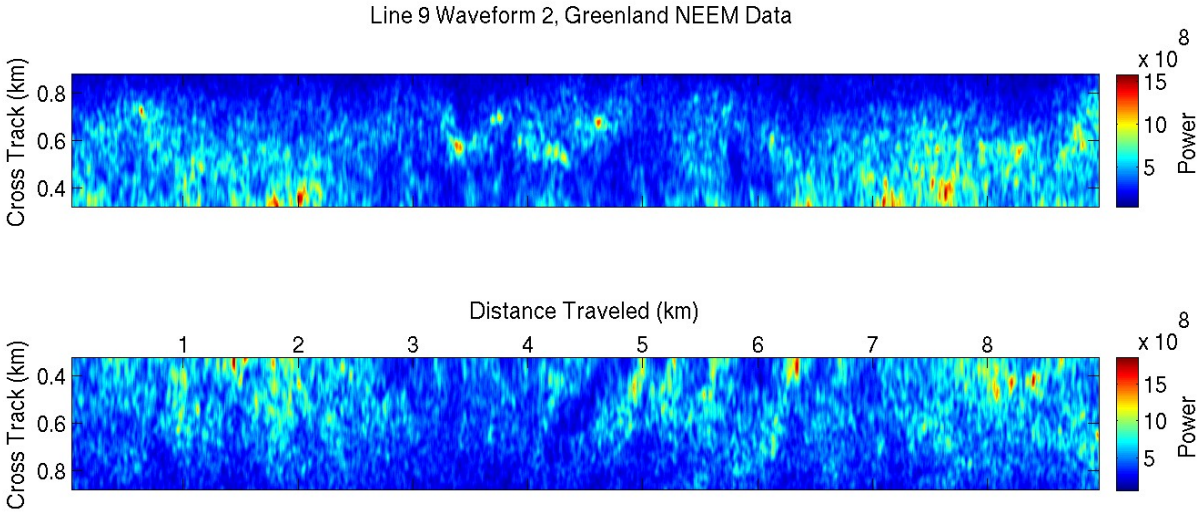

Figure 4.25: Side-looking SAR image before mean removal and accurate georeferencing

To take out the effects of both the beam pattern and the target's backscattering characteristics the data were averaged across the entire swath to produce an estimate of the beam pattern plus backscatter versus off nadir distance. A plot of those trends are below.

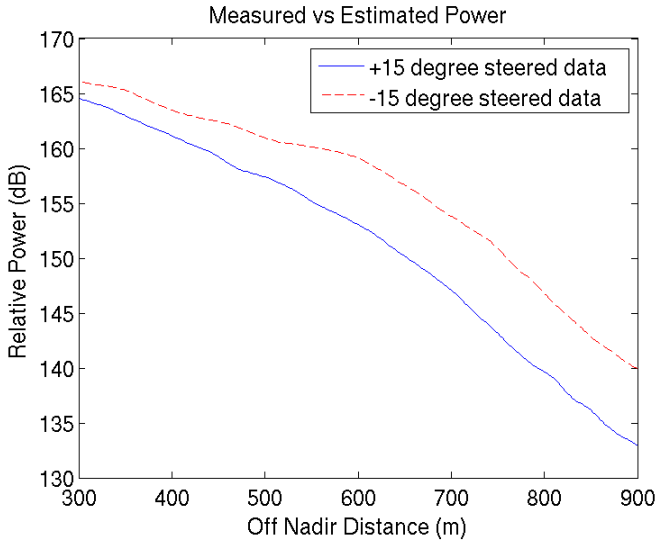

Figure 4.26: Mean power for line 9

We notice that there is a significantly higher (3 – 6 dB) higher return from one side than

the other. This is most likely due to imbalance in the transmitter radiation pattern. The mean off nadir power is examined further in chapter 5.

After the removal of the mean off-nadir power, the image becomes much more uniform across the entire swath as seen in figure 4.27.

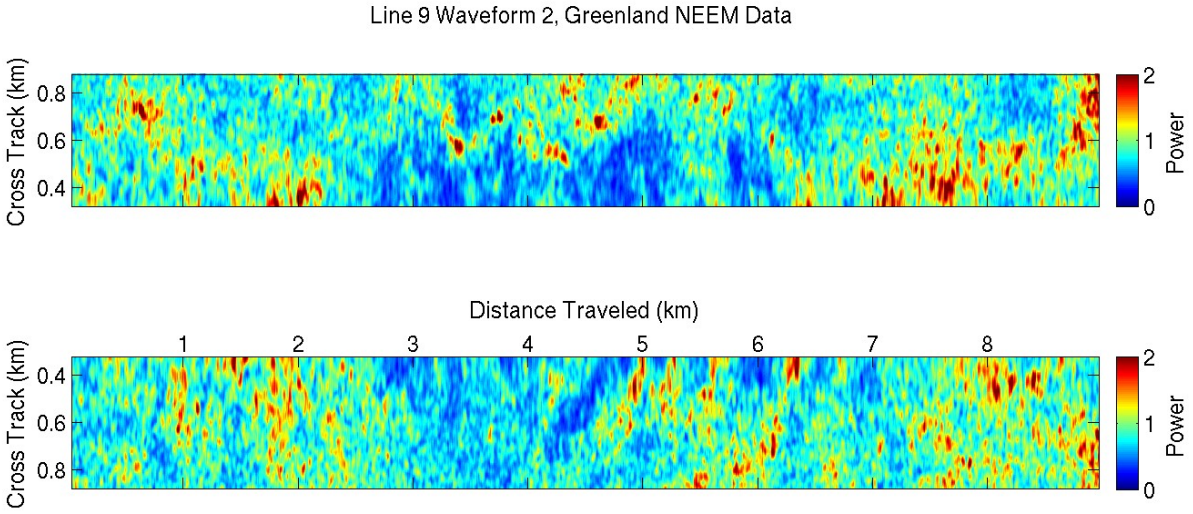

Figure 4.27: Side-looking SAR image after mean removal, before accurate georeferencing

To verify that the beam steering is working as expected the left and right images were converted to dB then subtracted from each other. The maximum difference between the left and right images was greater than 16 dB which is acceptable for this work. The results are shown in figure 4.28 below.

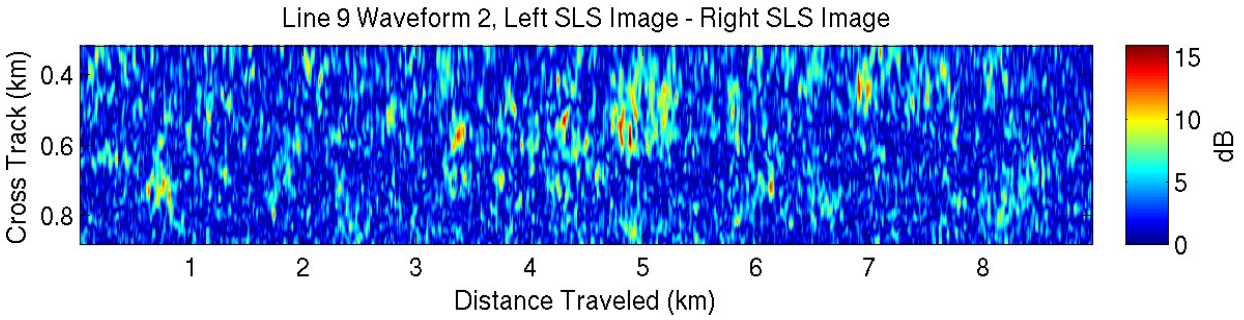

Figure 4.28: Difference between left and right side-looking SAR images

4.2.14 Coherence Measurements Between Side-Looking Images

Since we have two TX antennas at different locations, we can form two images looking at the same location, either left or right. From these two complex images we form a coherence map. A coherence map is calculated by multi-looking on a 6 pixel by 8 pixel basis using the formula:

$$\gamma = \left| \frac{E\{s_1 \cdot s_2^*\}}{\sqrt{(E\{|s_1|^2\} \cdot E\{|s_2|^2\})}} \right| \tag{9}$$

where γ is the coherence measure from 0 to 1, s_1 and s_2 are the appropriate 6 pixel by 8 pixel subset of the same location from the two transmitters. Coherence measures are discussed more in the next section

4.2.15 Image Registration

Line 7 was examined to provide the initial pixel shift values. This was then compared to several other lines with consistent results. For the negative 15 degree looking line the initial coherence averaged across the image was: 0.8915. Graphically the coherence values from 0.5 to 1 look

can be seen in figure 4.29.

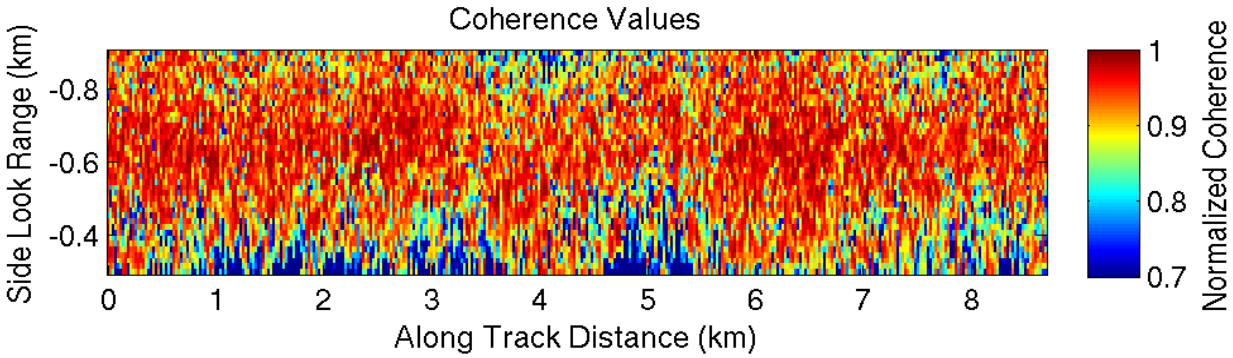

Figure 4.29: Line 7 (-15°) coherence values before registration

0.8915 is a very good coherence across the image however for completeness both coarse and fine scale registration was performed. The coarse scale values are:

Table 3: Coarse scale coherence values for -15°

Pixel Shift	Average Coherence
-3.0	0.88880
-2.0	0.89995
-1.0	0.90223
0	0.89514
1.0	0.87854
2.0	0.85371
3.0	0.82202

Based off the results from Table 3, fine registration was performed for pixel shifts between -3.0 and 0.0 using a 0.1 pixel spacing.

Table 4: Fine scale coherence values for -15°

Shift Value	Average Coherence	Shift Value	Average Coherence
-3.0	0.888798	-1.4	0.902424
-2.9	0.890298	-1.3	0.902514
-2.8	0.891716	-1.2	0.902512
-2.7	0.893050	-1.1	0.902417
-2.6	0.894299	-1.0	0.902231
-2.5	0.895459	-0.9	0.901953
-2.4	0.896532	-0.8	0.901583
-2.3	0.897517	-0.7	0.901119
-2.2	0.898414	-0.6	0.900558
-2.1	0.899224	-0.5	0.899900
-2.0	0.899947	-0.4	0.899144
-1.9	0.900584	-0.3	0.898289
-1.8	0.901134	-0.2	0.897336
-1.7	0.901594	-0.1	0.896286
-1.6	0.901963	0.0	0.895140
-1.5	0.902240		

As seen in table 4, the optimal pixel shift for Line 7 steered to -15 degrees is -1.3 pixels. The coherence values after fine scale registration are shown in figure 4.30.

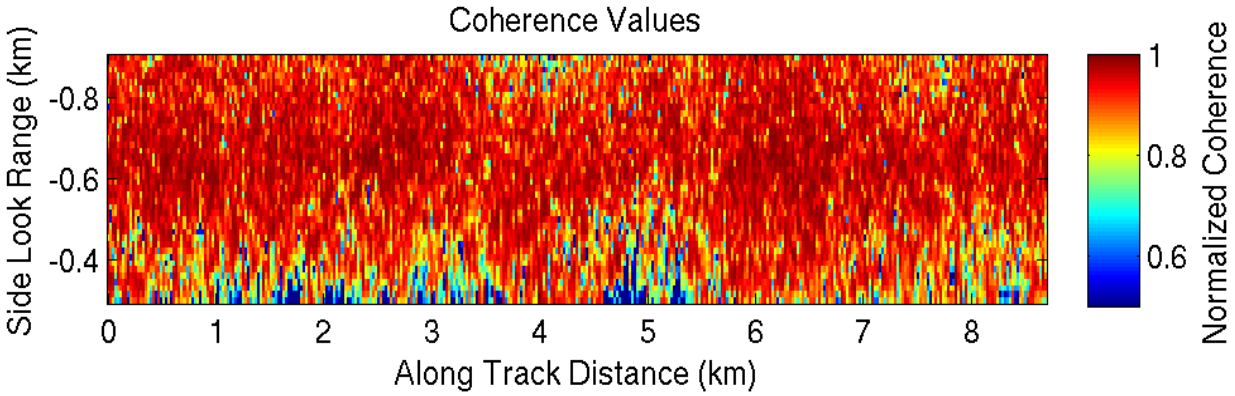

Figure 4.30: Line 7 (-15°) coherence after fine registration with -1.3 pixel shift

For comparison these values were then compared to the positive 15 degree looking images for line 7. These images were shifted from 0.0 to 3.0 using 0.1 spacing.

Table 5: Fine scale coherence values for +15°

Shift Value	Average Coherence	Shift Value	Average Coherence
0.0	0.891097	1.6	0.901192
0.1	0.892399	1.7	0.901067
0.2	0.893613	1.8	0.900855
0.3	0.894737	1.9	0.900555
0.4	0.895770	2.0	0.900168
0.5	0.896712	2.1	0.899696
0.6	0.897563	2.2	0.899138
0.7	0.898323	2.3	0.898492
0.8	0.898993	2.4	0.897756
0.9	0.899574	2.5	0.896930
1.0	0.900067	2.6	0.896013
1.1	0.900475	2.7	0.895004
1.2	0.900795	2.8	0.893905
1.3	0.901028	2.9	0.892715
1.4	0.901172	3.0	0.891434
1.5	0.901227		

For the positive 15 degree images a pixel shift of 1.5 was optimal as opposed to a shift of -1.3 for the negative 15 degree looking image. For this scenario, one pixel corresponded to 2.5 m, representing an estimated baseline of 3.25 m to 3.75 m, which was close to the actual 3.658 m baseline, as was expected.

The coherence is affected by three main factors [Rodriguez and Martin 1992][Zebker and Villasenor 1992]

$$\gamma = \gamma_{SNR}\gamma_H\gamma_a \tag{10}$$

where γ_{SNR} is the decorrelation caused by the SNR from the two looks, γ_H is the decorrelation due to fact that slight different filters with possibly different impulse responses were used during processing, and γ_a is the temporal scene coherence. If we assume that the effects from γ_H and γ_a are minimal we can use our calculated coherence to predict a minimal SNR that would cause the measured coherence. The relationship between SNR and γ_{SNR} is [Just and Bamler 1994] [Zebker and Villasenor 1992]:

$$\gamma_{SNR} = \frac{1}{\sqrt{(1+N_1/S_1)(1+N_1/S\ )}} \tag{11}$$

where N_1 is the noise power and S_1 and S are the signal power from images 1 and 2 respectively. Assuming $S_1 = S_2$ we can say:

$$\gamma_{SNR} = \frac{1}{\sqrt{(1+N_1/S_1)^2}}$$

$$\gamma_{SNR} = \frac{1}{1+N_1/S_1}$$

solving for S_1/N_1 we get:

$$S_1/N_1 = \frac{\gamma_{SNR}}{1-\gamma_{SNR}} \tag{12}$$

for this case S_1/N_1 is our predicted worse case SNR assuming all the decorelation is due to just SNR. Looking at our average coherence across the swath from 300 to 900 m off nadir we get figure 4.31.

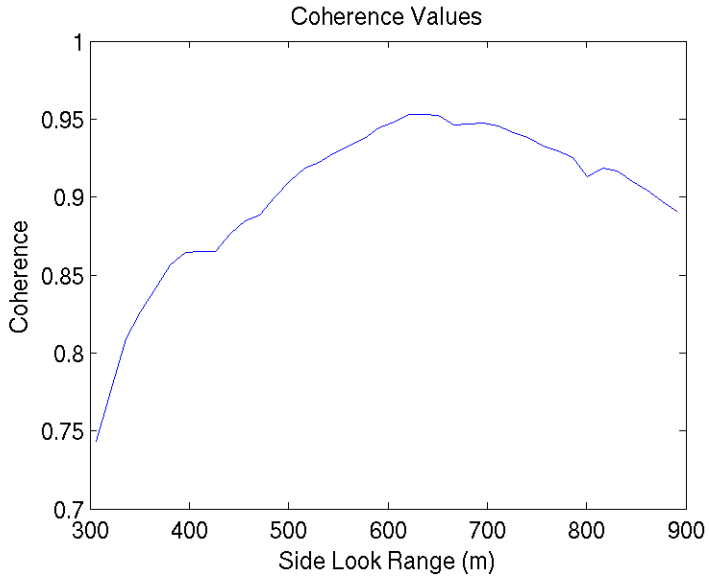

Figure 4.31: Coherence values versus cross track

Using these data to generate a predicted, worst case, SNR using equation 12 we get figure ##.

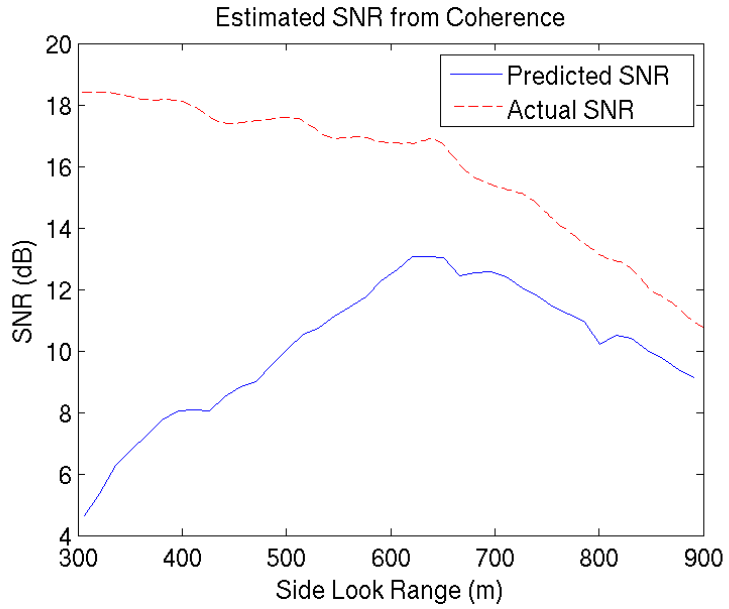

Figure 4.32: Predicted worst case SNR from coherence data

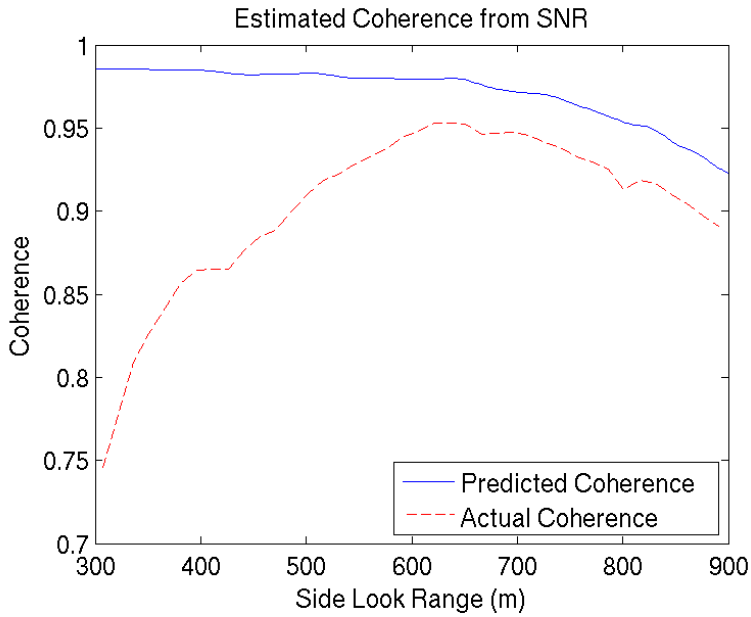

Figure 4.33: Predicted coherence from SNR

Figures 4.32 and 4.33 show two different ways to look at the coherence and the SNR. Figure 4.32 shows predicted SNR based of the measured coherence and figure 4.33 shows the

predicted coherence based off the measured SNR. Figure 4.32 provides us with a bound that shows that we are getting at least 8 dB of SNR from 400 m to 900 m based off the measured coherence across our swath. Also we see that the predicted SNR and actual SNR follow the same trend from 600 to 900 m. The most likely reason for the lower predicted SNR from 300 to 600 m is because we are actually limited by left/right isolation. This same trend is seen in the predicted versus measured coherence.

4.2.16 Interferogram Generation

With two complex finely registered images a complex interferogram was created. This was done using a pixel-by-pixel multiplication with the complex conjugate.

$$Z = Z_1(x, y) \cdot Z_2(x, y)^* \tag{13}$$

Where Z is the interferogram values and Z_1 and Z_2 are the values from the two different transmitters. A plot of the values at this level should show fringes caused by interaction of the phases between the two images.

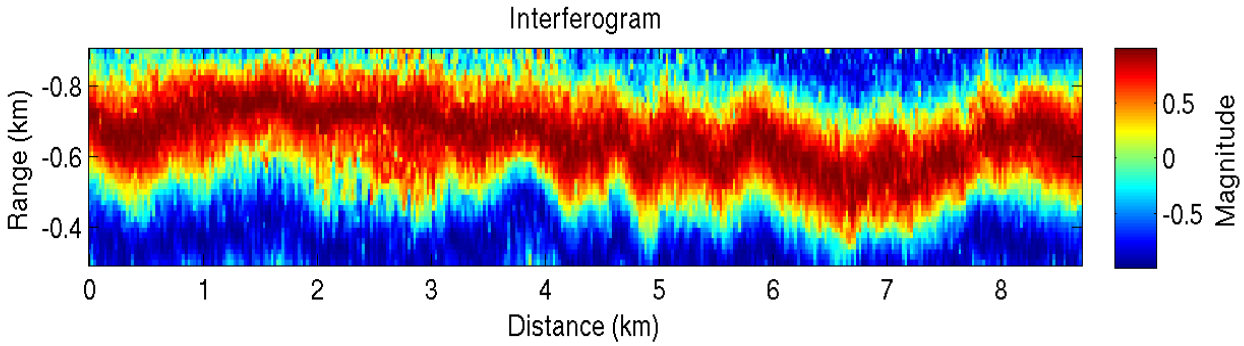

Figure 4.34: Line 9 (-15°) steered interferogram showing varying fringes

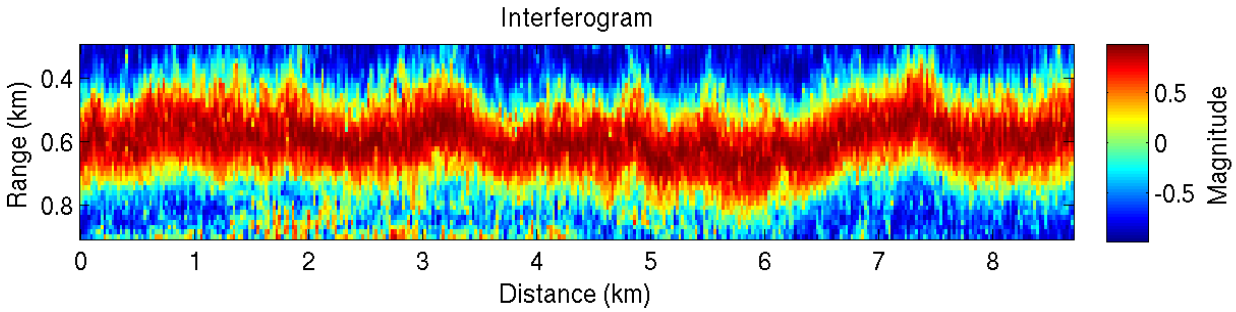

Figure 4.35: Line 9 (+15°) steered interferogram showing varying fringes

As seen in figures 4.34 and 4.35 there are fringes present in the interferogram corresponding to varying off nadir topography.

4.2.17 Interferometric Phase Calculation

An additional, more valuable product is the unwrapped interferometric phase plot. The phases are calculated using:

$$\delta_\phi = \arctan \frac{\Re\{Z(x,y)\}}{\Im\{Z(x,y)\}} \tag{14}$$

where δ_ϕ represents the is the difference in phase between looks from the two transmitters. Another way to think of this is as the angle of the coherence γ .

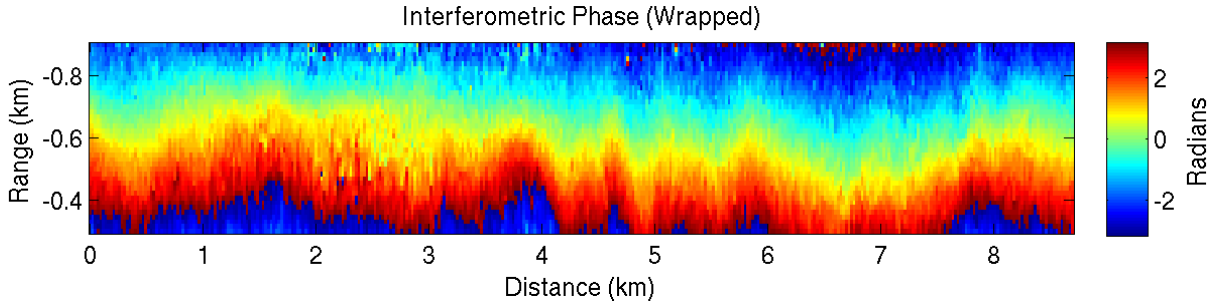

Figure 4.36: Line 9 (+15°) steered wrapped interferometric phase

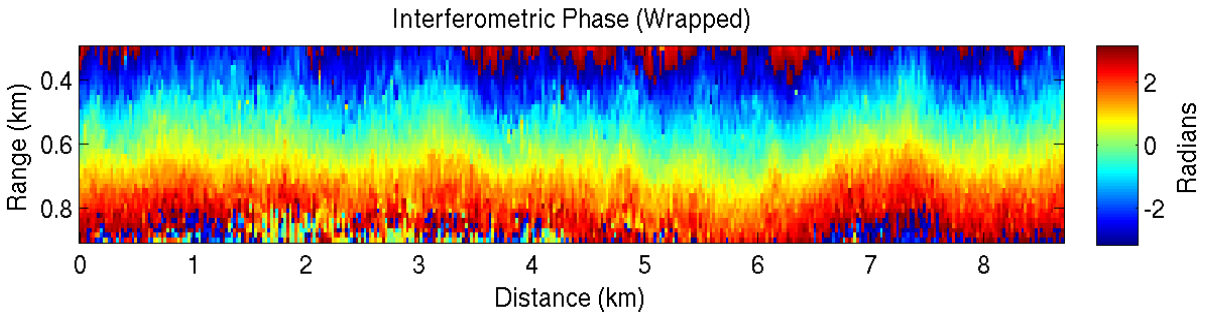

Figure 4.37: Line 9 (+15°) steered wrapped interferometric phase

As seen in figures 4.36 and 4.37 the phase wraps, therefore it is necessary to unwrap the phase provide an absolute phase difference.

4.2.18 Phase Unwrapping

After several unsuccessful phase unwrapping tries with different tools due to outlying points and/or degraded SNR in different areas, a phase unwrapping algorithm was implemented where the data were shifted 180 degrees (so the wrapping was now in the center of image) and the transition, or wrapping region, was detected. The unwrapped image was then put together piecewise.

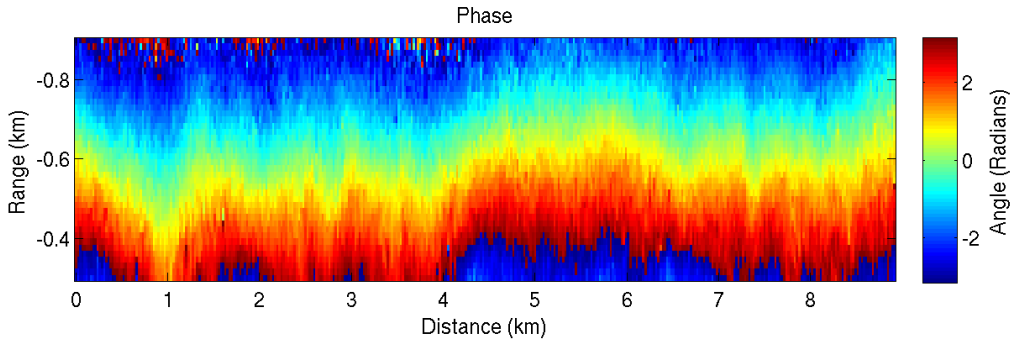

Figure 4.38: Line 9 (+15°) phase values

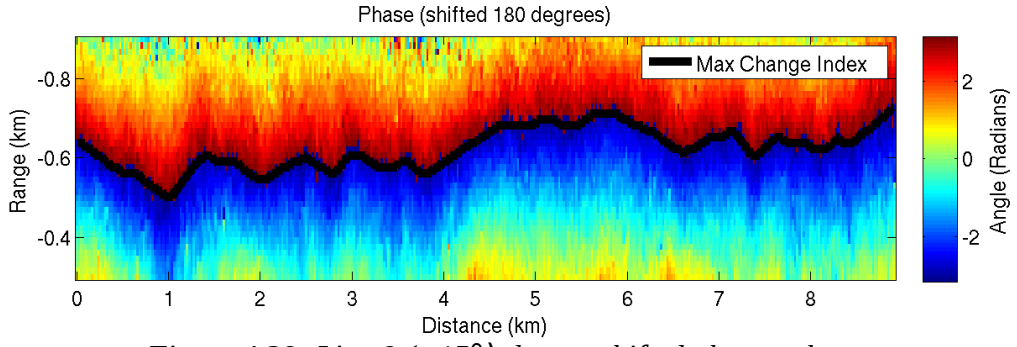

Figure 4.39: Line 9 (+15°) degree shifted phase values

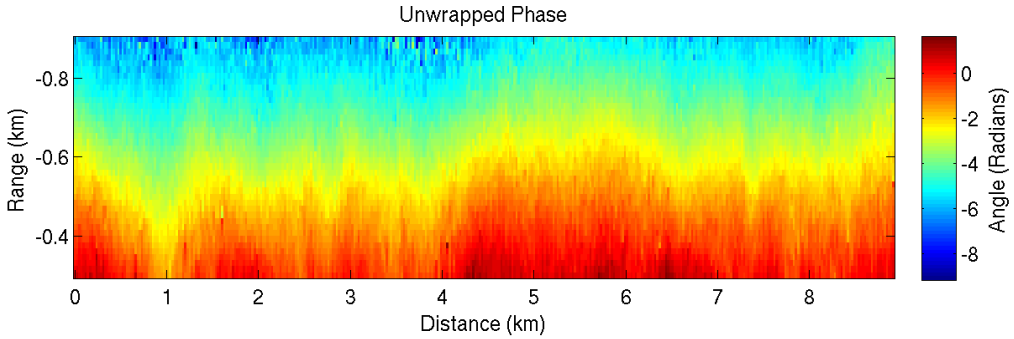

Figure 4.40: Line 9 (+15°) degree unwrapped phase values

After the unwrapping process we now have an absolutely referenced phase difference between the two transmitters as seen in figure 4.40.

4.2.19 Varying Heading Correction

The next step is to create a height map from the unwrapped phase data. However to accurately georeference these data we need to know the platform heading at any given time so the data can be projected. The heading was calculated from the the GPS data and then filtered to remove inaccuracies. The calculated heading for line 1 is shown in figure 4.41, and the filtered heading in figure 4.42.

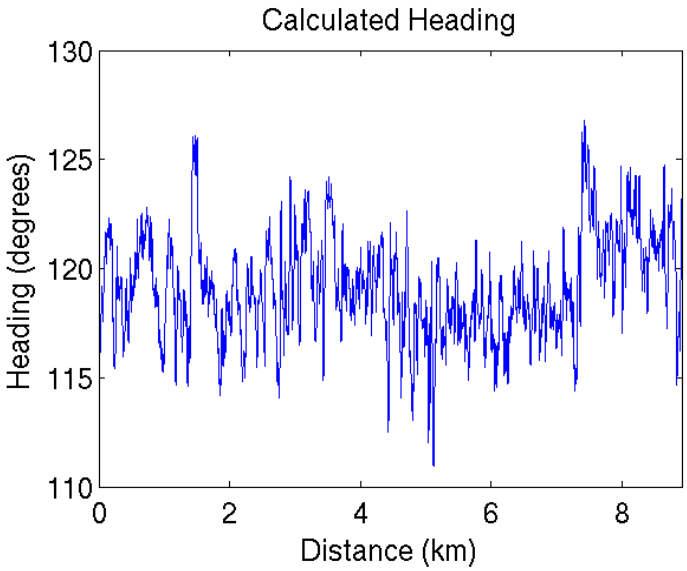

Figure 4.41: Heading calculated from GPS

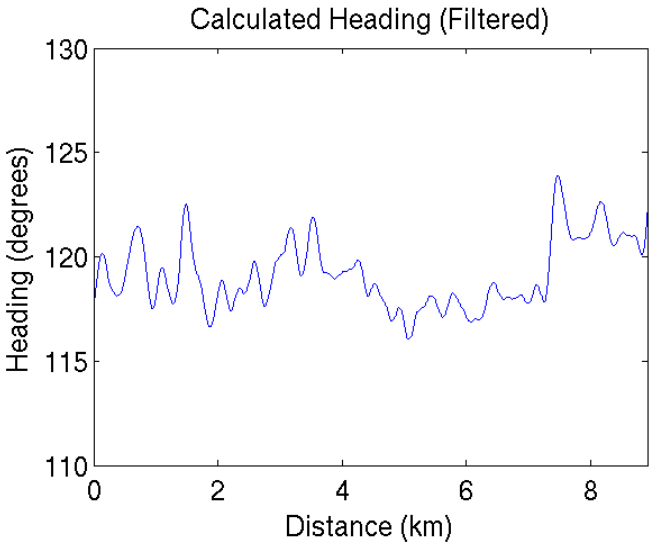

Figure 4.42: Heading calculated from GPS after filtering

After filtering the heading is well behaved. The filtered heading was used to project the data in the cross track direction for the height DEM.

4.2.20 Height Calculation

A swath of height values was calculated using the equation 7 derived in chapter 2 relating the unwrapped phase values to the height values:

$$h = H - R_1 \cos\left[\sin^{-1}\left[\frac{-\left(\frac{\delta_\Phi}{a\,k} + R_1\right)^2 + R_1^2 + B^2}{2R_1 B}\right]\right]$$

where h is the height of the terrain, H is the height of the platform, R_1 is the calculated range to the target, δ_Φ is the phase between the two transmitters (as shown in the unwrapped phase image), k is the wave-number based off a center frequency of 150 MHz, and a is 1 for this case with two transmitters and a common receiver. The height values for the +15 degree beam for line 9 is shown in figures 4.43 and 4.44.

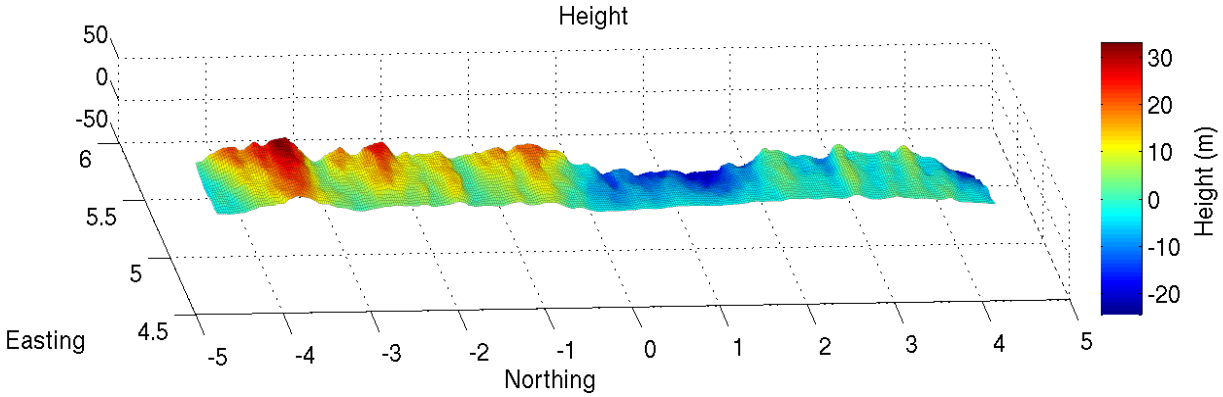

Figure 4.43: Line 9 (+15°) degree height swath

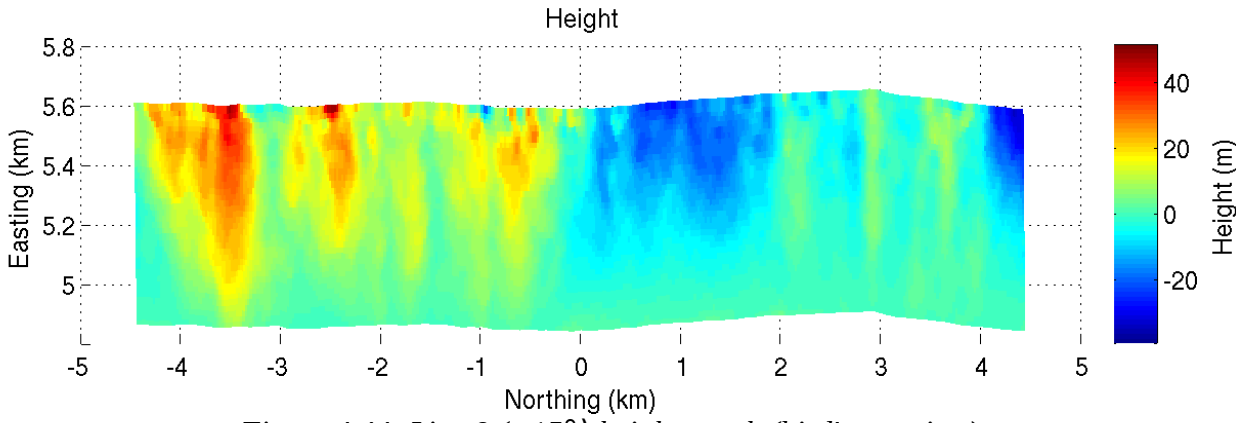

Figure 4.44: Line 9 (+15°) height swath (bird's eye view)

The resulting swath of data is about 700 m wide, however we see some noise on the upper couple of rows, and height underestimating on the bottom edge of figure 4.44. Therefore the top 5 rows and bottom 3 rows are removed before mosaicing.

4.2.21 Calculating Surface Height

Up till now all the values calculated have been thickness values, which are important and valuable but not as valuable as an accurate basal digital elevation map (DEM) relative to mean sea level (msl). To create a DEM we need knowledge of the surface topography over the surveyed area. The GPS data that were collected on the radar platform were not differential GPS. This led to jumps of up to 10 m in the GPS data as different satellites where acquired and lost. If these were not corrected then they would adversely affect the basal DEM. Therefore a smoothing filter was created to reduce the effect of these jumps. The filter takes the mean of all the points in a 1.5 km radius to determine the best estimate for the surface value at that point.

Figures 4.45 and 4.46 show the surface before and after filtering.

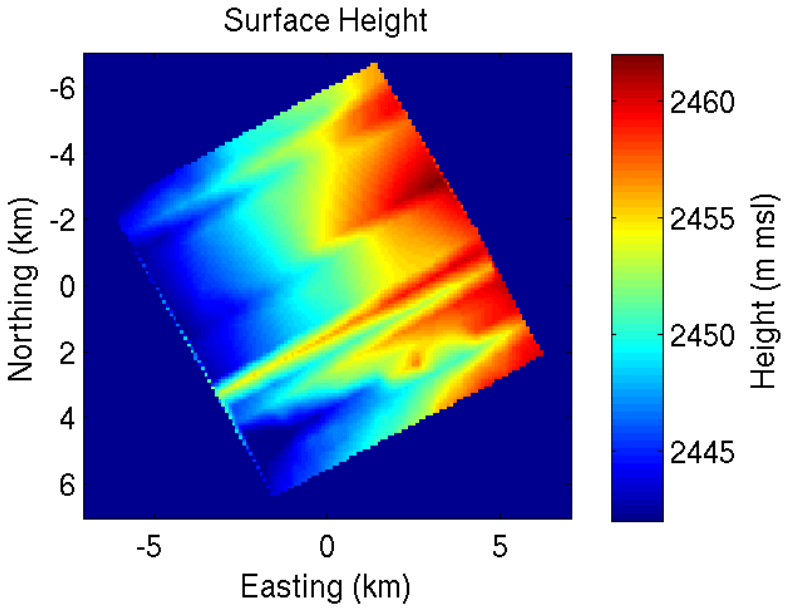

Figure 4.45: Surface elevation data with no filtering

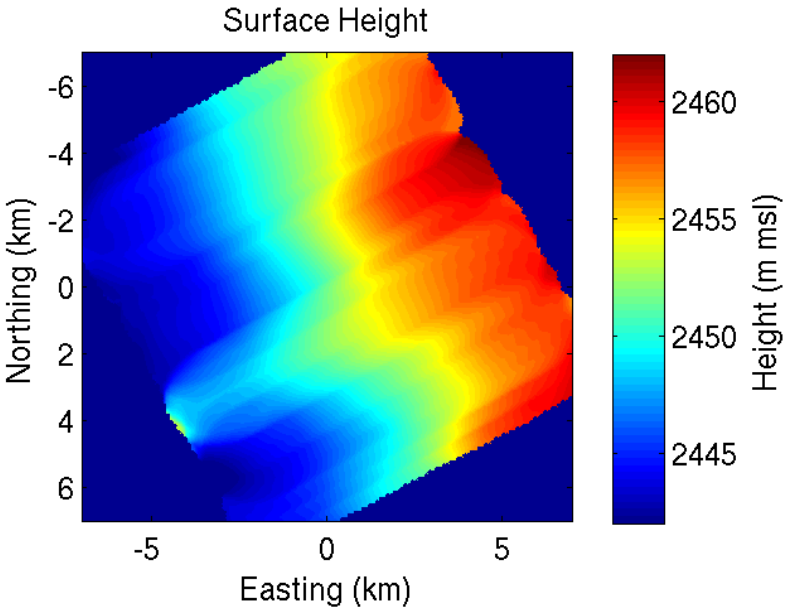

Figure 4.46: Surface elevation data after filtering

After the 2D smoothing filter the surface elevation changes are more realistic for this

area, and should not create any artifacts in the DEM.

4.2.22 Mosaic Multiple Lines

At this point there are more than 40 individual lines, with about 30% of these data overlapping at least one other line. To mosaic these together several steps were required. First it was necessary to interpolate the data to a common grid. Therefore a 7 km by 7 km grid with 25 m spacing was created around the NEEM drill site where the data lines were centered. To go along with this the off-nadir distance was also interpolated to the same grid for all these points which will be used to create a cost for each overlapping point.

To optimize the combining of multiple lines together a sine function from 30 to 150 degrees was fit to the values of 100 m to 800 m off nadir, where most of the data were located. This weighted the data close to nadir and the data far from nadir less than those data in the center of the swath as those appear to have the best SNR. This provides a method for gradually fading out data from one line to the other leading to less abrupt transitions between overlapping segments. The final curve from 0 to 900 meters is shown in figure 4.47.

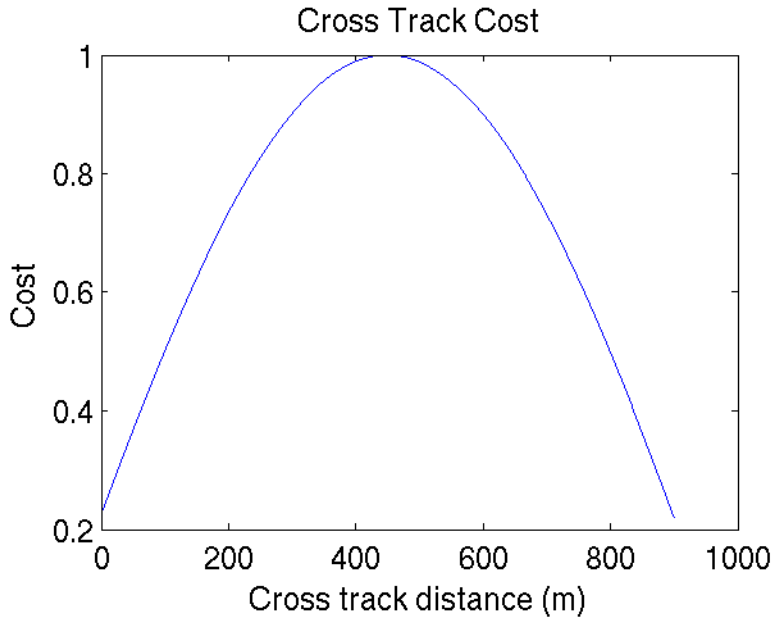

Figure 4.47: Cross track cost

Using this algorithm a mosaic of all the lines was created as seen in figures 4.48 and 4.49. The white pipe/circle corresponds to the NEEM drill location.

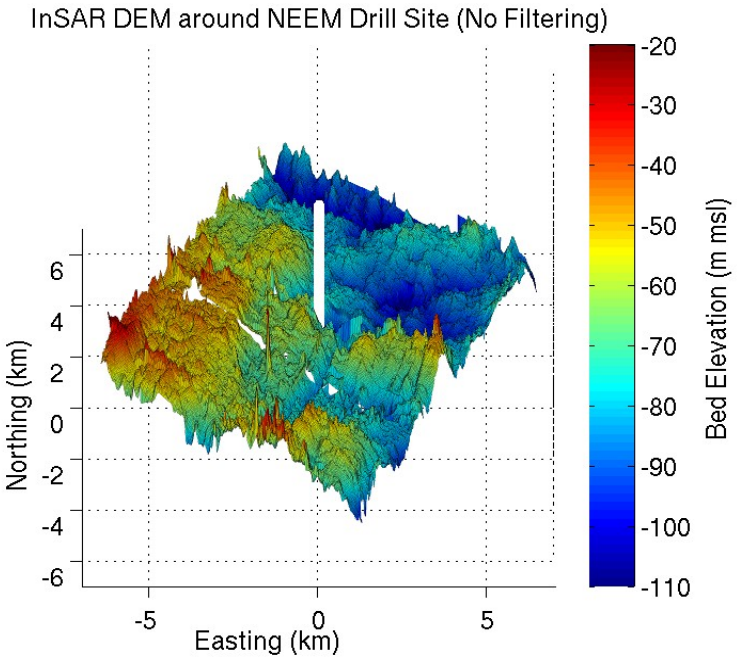

Figure 4.48: InSAR mosaic with no filtering

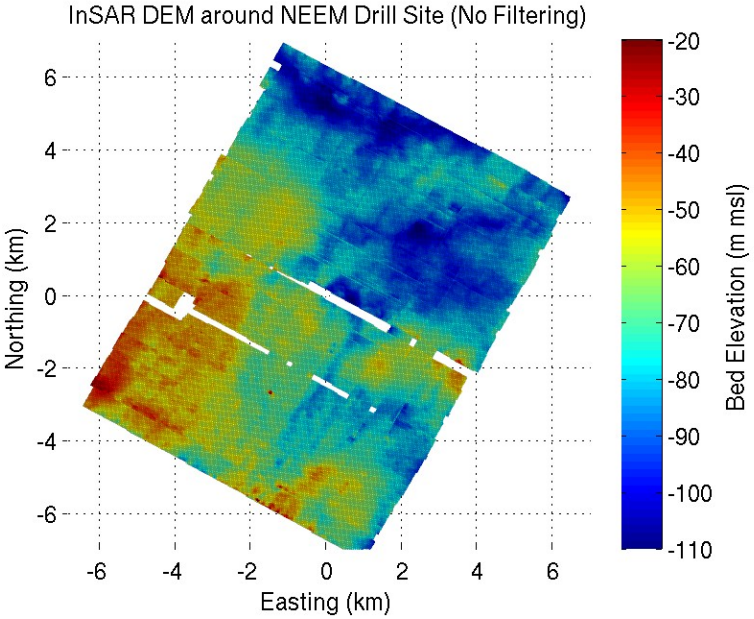

Figure 4.49: InSAR mosaic with no filtering (bird's eye view)

To remove point target artifacts a 5 point by 5 point median filter was applied across the interpolated mosaic. Additionally this has somewhat of a smoothing effect. Further a 7 point by 7 point 2D filter was applied to remove some of the high frequency artifacts in the image. This lead to a final image as shown in figures 4.50 and 4.51.

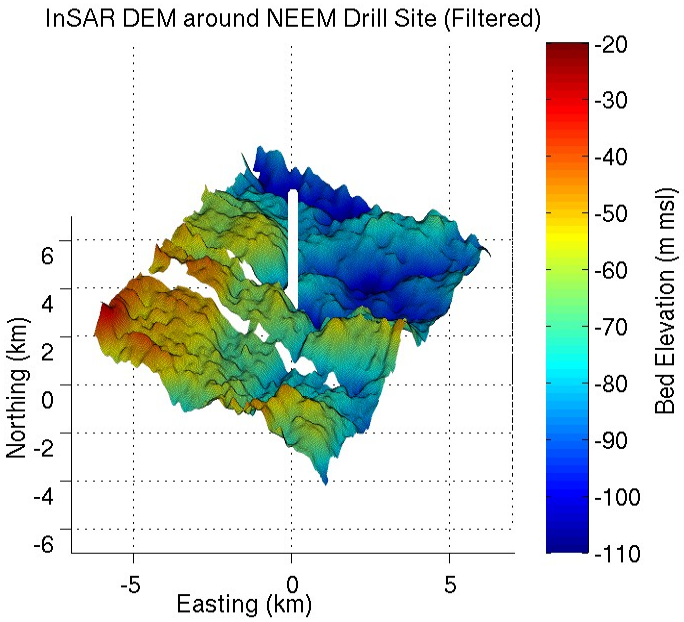

Figure 4.50: InSAR mosaic with filtering

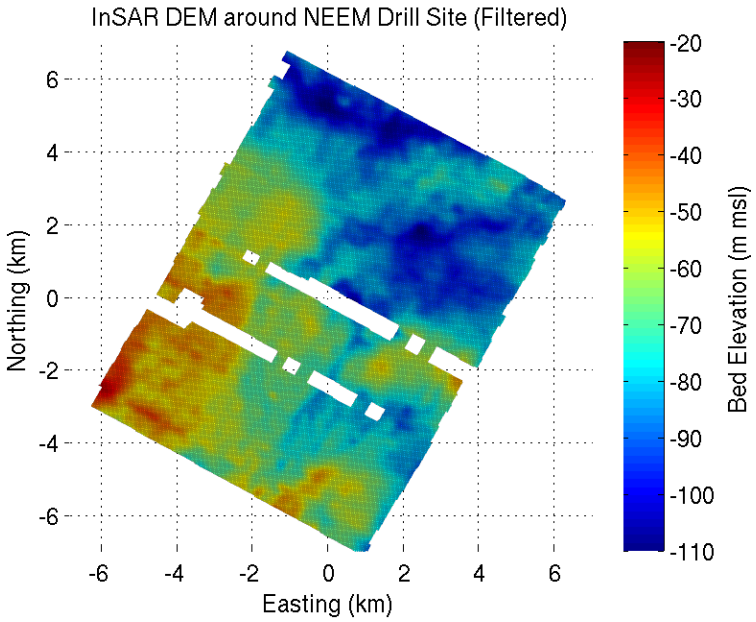

Figure 4.51: InSAR mosaic after filtering (bird's eye view)

As seen in the previous figures, a gap in the mosaic was present where GPS data were lost for multiple lines. Over this area a Delaunay triangulation algorithm was used to fill in the gaps. While not optimal this provides complete coverage across the entire area as seen in figures 4.52 and 4.53.

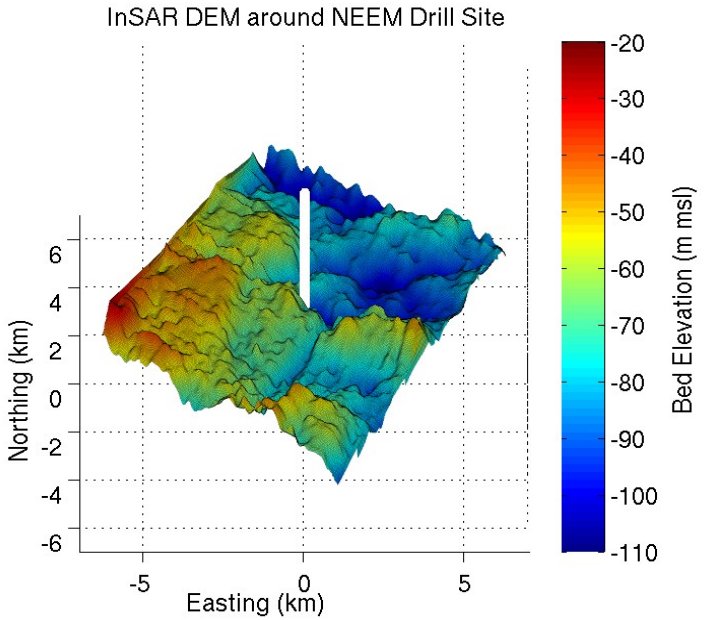

Figure 4.52: InSAR mosaic after filtering and interpolation

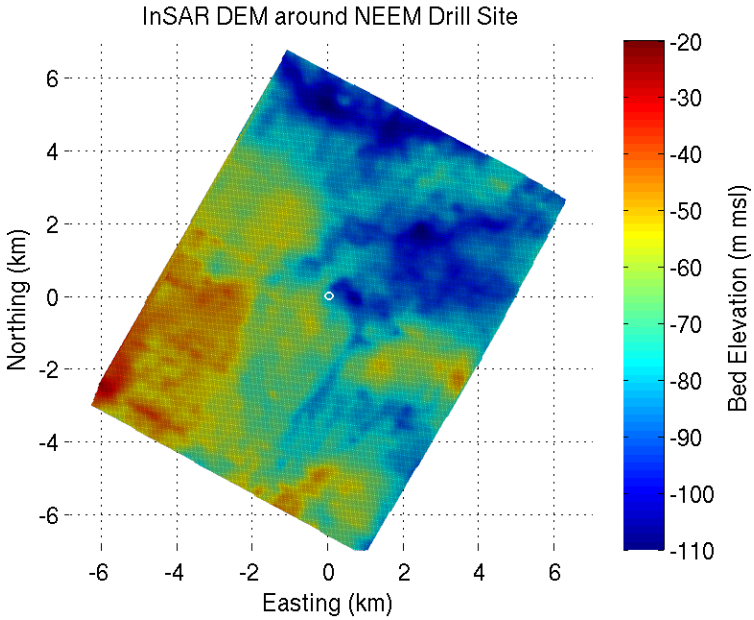

Figure 4.53: InSAR mosaic after filtering and interpolation (bird's eye view)

After mosaicing, filtering, and interpolation the final DEM looks very consistent across the entire area. It should also be noted that the calculated depth at the drill site location using this map was 2536 m, the actual drill site depth reached on July 27th 2010 was 2537.36 m.

4.2.23 Before and After

At this point a side by side comparison with original coarse resolution image would be interesting.

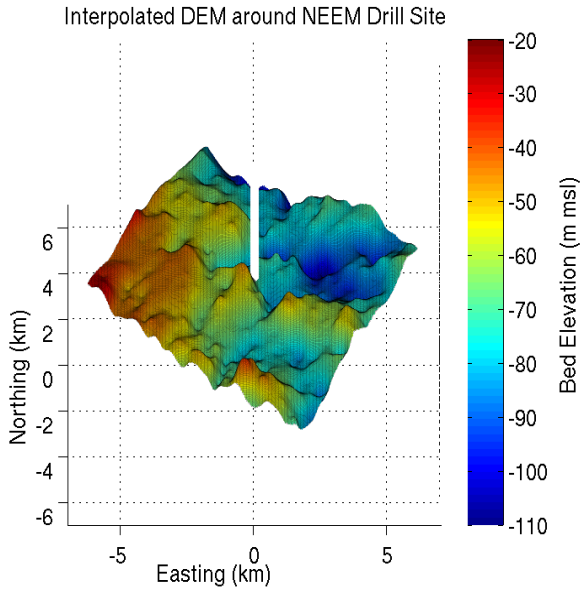

Figure 4.54: DEM without using InSAR

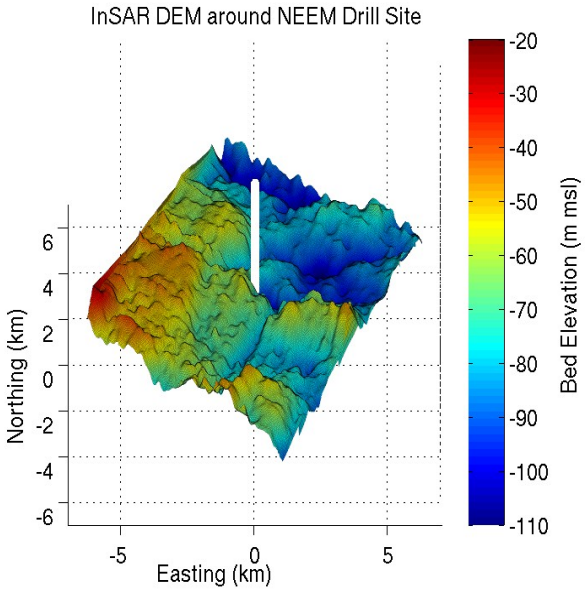

Figure 4.55: DEM using InSAR product

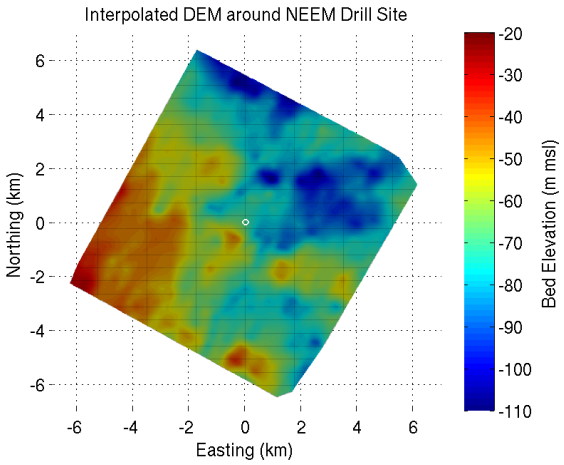

Figure 4.56: DEM without using InSAR (bird's eye view)

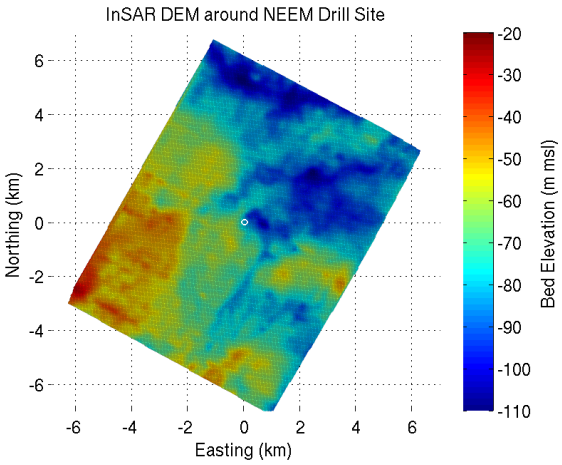

Figure 4.57: DEM using InSAR (bird's eye view)

There is definitely better resolution for the InSAR DEM than the basic interpolated DEM. The results aren't as dramatic as they could be though since there is not a whole lot of topography in this area. But we can see more features on the InSAR DEM and we gain an extra 800 m on both the top and bottom edges due to the swath width, however about 200 m on the left and right sides is lost due to filtering. To highlight the additional features seen after the InSAR processing the before and after images were subtracted from one another. This resulted in figures 4.58 and 4.59.

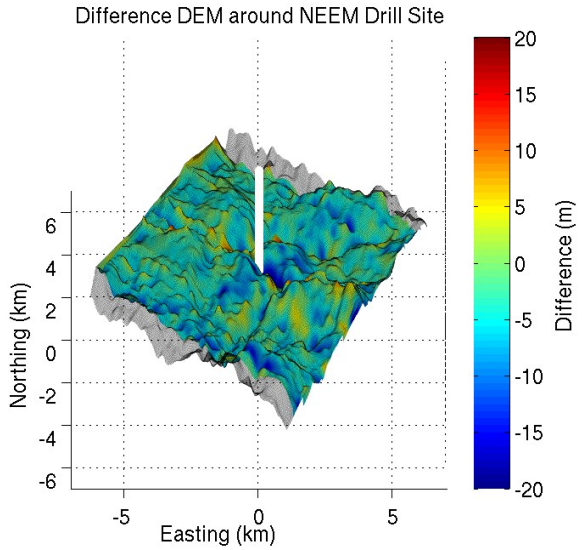

Figure 4.58: Difference between original and InSAR DEMs

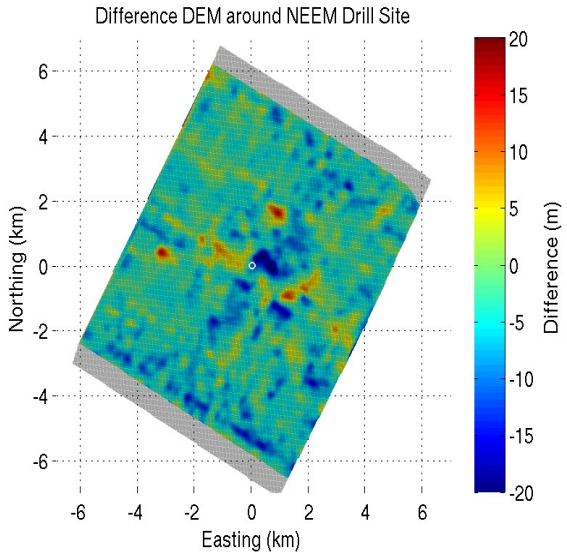

Figure 4.59: Difference between original and InSAR DEMs (bird's eye view)

In an area with coarser sampling and larger topographical features the differences would be more dramatic, but we can still see quite a few features that were not present before the InSAR processing.

4.2.24 Theoretical Height Errors

To calculate the theoretical height errors for SNR > 10 dB we can use the formula:

$$\Phi_{err} \approx \frac{1}{\sqrt{2\,SNR}} \tag{15}$$

where Φ_{err} is in radians. However our worst case SNR would be about 6 dB (looking back at our steered beam power data). From [Ronnau et al. 1994] a 6-dB SNR would create a phase error of approximately 20 degrees. For a target 2550 m deep and 1000 m off nadir with a phase error of 20 degrees that corresponds to a height error of 17.9 m as calculated below using equation 7 from chapter 2.

$$h = H - R_1 \cos\left[\alpha + \sin^{-1}\left[\frac{-\left(\frac{\delta_\Phi}{a\,k} + R_1\right)^2 + R_1^2 + B^2}{2 R_1 B}\right]\right]$$

Modifying this to include a phase error term we have:

$$h = H - R_1 \cos\left[\alpha + \sin^{-1}\left[\frac{-\left(\frac{\delta_\Phi + \Phi_{err}}{a\,k} + R_1\right)^2 + R_1^2 + B^2}{2 R_1 B}\right]\right]$$

where Φ_{err} is the phase error

$$h = \quad -2739.07 \cos\left[\sin^{-1}\left[\frac{-\left(\frac{-7.085 + 0.349}{1 * 5.5758} + 2739.07\right)^2 + 2739.07^2 + 3.658^2}{2 * \quad . \quad * 3.658}\right]\right]$$

$$h = -17.9\,m$$

Therefore for a target 1000 m off nadir, a 20 degree phase error causes a 17.9 m error in the height estimate. This is a worst case scenario, figure 4.57 shows what a 20 degree phase error causes for various cross track ranges, compared with an SNR of 13 dB causing a 9 degree phase error.

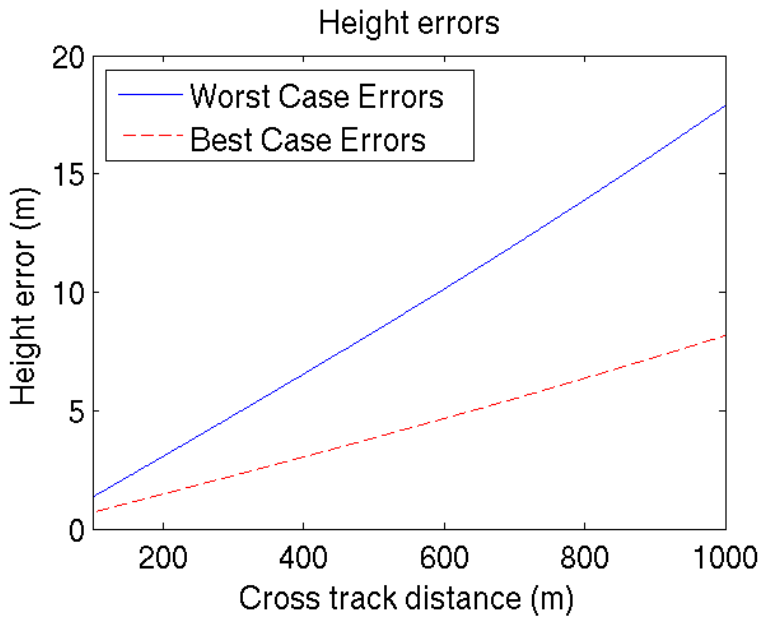

Figure 4.60: Height errors caused by 20° (worst case) and 9° (best case) phase errors

Based off our SNR we should expect 5 to 15 m height errors for most of our data as seen in figure 4.60.

4.2.25 Verification of Height Estimates

To verify the accuracy of the height estimates, comparisons were done between crossing and adjacent lines. The lines used for the crossing lines comparison were line 7, and crossline 1. The scatter plot of errors is shown in figure 4.58 and graphically in figure 4.59.

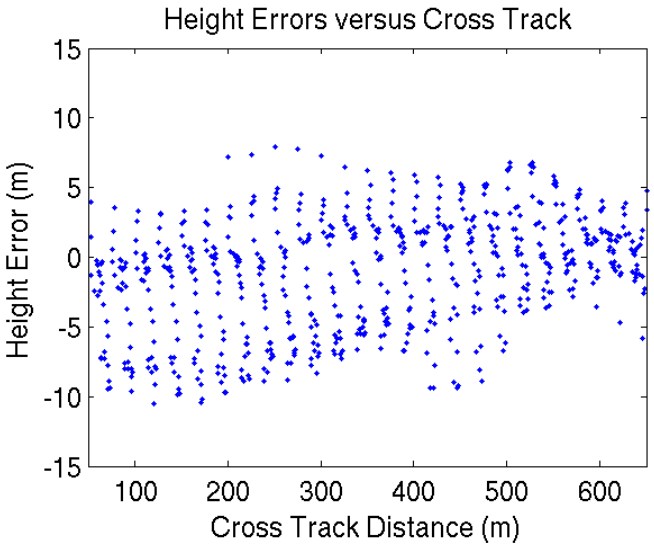

Figure 4.61: Height errors for crossing lines

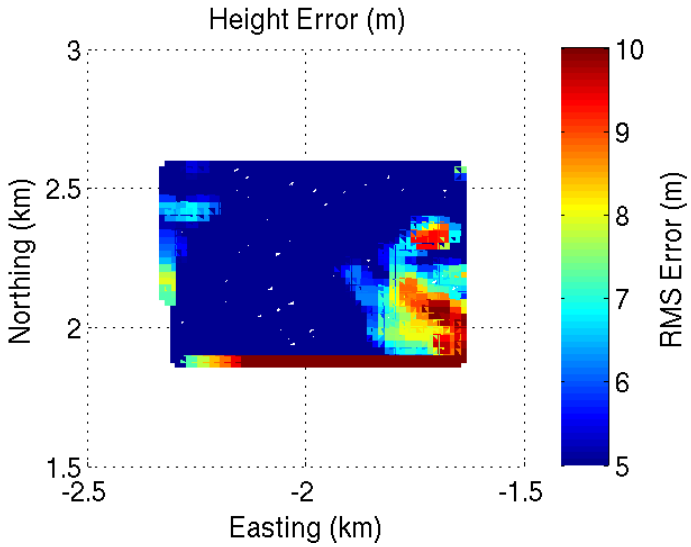

Figure 4.62: Height error of crossing lines

For the crossing lines an RMS error of 4.7 m was calculated over the overlapping section with more than 96% of the data less than 10 m in error.

Lines 8 and 9 were used for analysis of adjacent lines with the scatter plot of errors shown in figure 4.63 and graphically in 4.64.

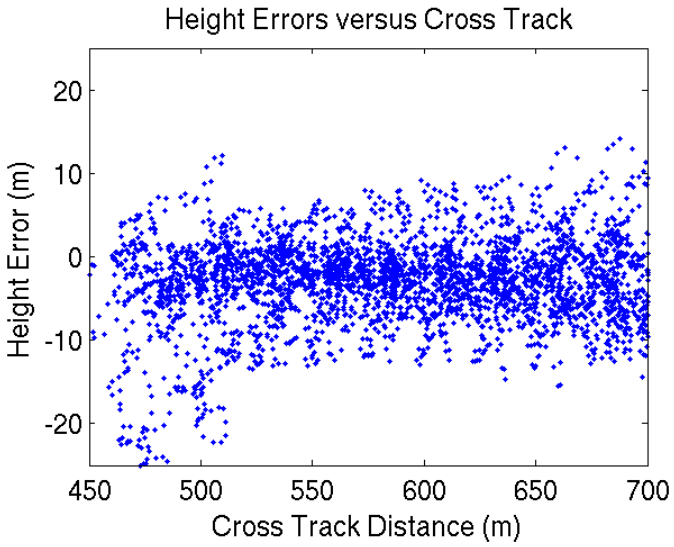

Figure 4.63: Height error of adjacent lines

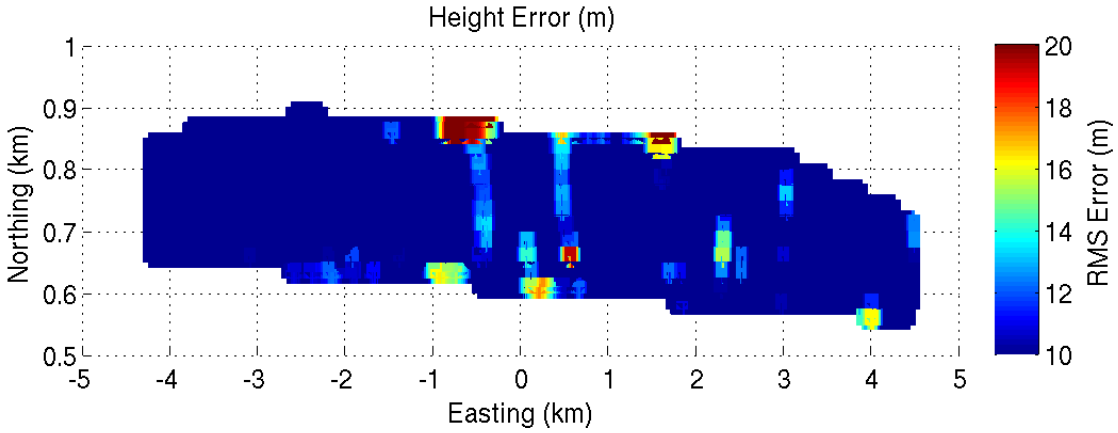

Figure 4.64: Height error of adjacent lines

The RMS error was 6.14 m for the adjacent lines with over 90% of the data less than 10 m in error. Overall the data matched well with no obvious trends of errors in cross track.

4.2.26 Comparison With Tomography

Another technique that can be used to create 3-D basal images is tomography using the MUSIC

algorithm, as shown in [Paden 2010]. This technique applies parametric estimation where the cross-track linear array is used for direction of arrival estimation. MUSIC uses the knowledge that for any given range shell there are only two returns, one from the left and the other from the right. Utilizing this a priori knowledge the direction to those two targets can be estimated very accurately. With the knowledge of the direction to the target you can re-project the data and create a 3-D image. To verify the InSAR results, they were compared with the tomography results. The 3-D tomography images are shown in figure 4.65 and 4.66.

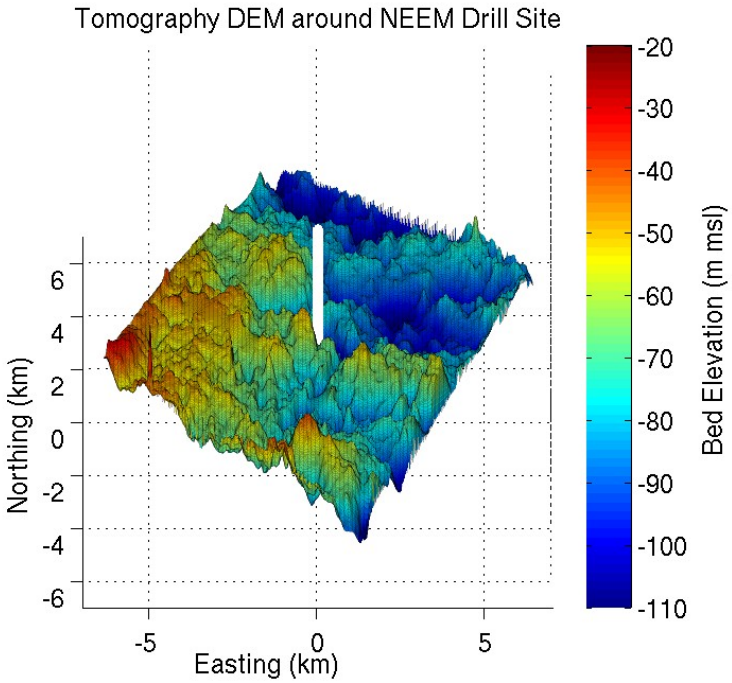

Figure 4.65: Tomography DEM

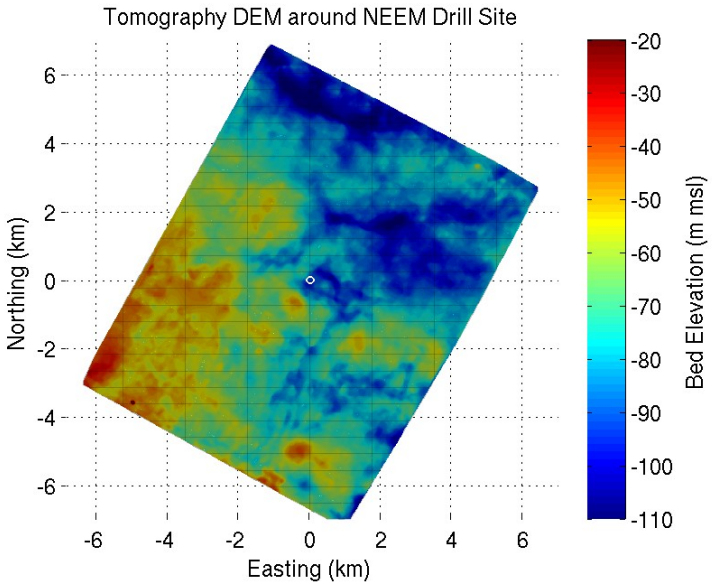

Figure 4.66: Tomography DEM around NEEM Drill Site (bird's eye view)

The difference between the tomography DEM and InSAR is shown in figures 4.67 and 4.68.

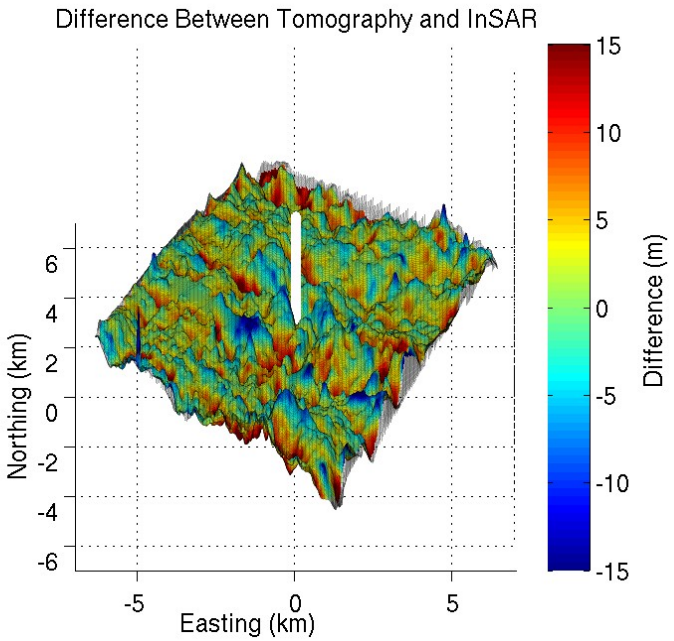

Figure 4.67: Difference between tomography and InSAR DEMs

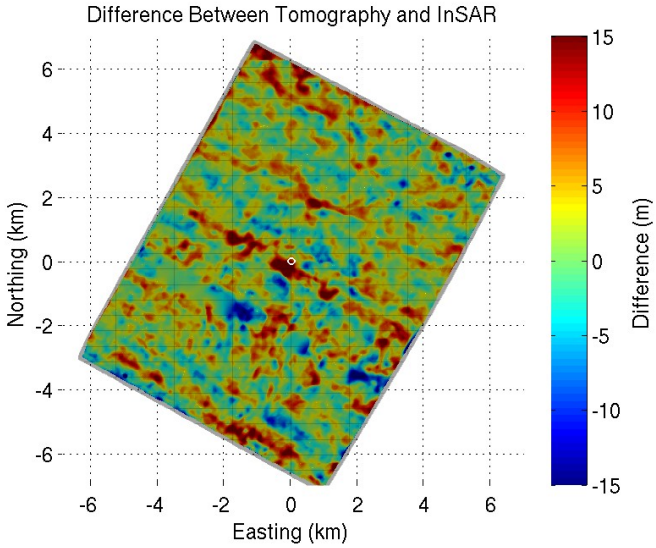

Figure 4.68: Difference between tomography and InSAR DEMs (bird's eye view)

In general the two techniques agree very well with an RMS error of 5 m It's interesting to

note that most of the large differences are on where the DEMs had to be interpolated due to the lost GPS data. The differences are most likely caused by the georeferencing for the two different techniques, which would slightly skew the two features being looked at and cause errors.

4.2.27 Overlay Reflectivity on DEM

Once a fine-resolution DEM produced using InSAR techniques is created it can be overlain with the reflected power. For simplicity the term reflectivity will be used, for the rest of the dissertation, to refer to the relative intensity of back scattered power from the basal interface. The various reflectivity values can give insight into the composition and roughness of various areas. Extraction of the composition and roughness will be discussed in the next chapter. Reflectivity maps were created from the lines looking northeast and southwest as seen in figures 4.69 and 4.70.

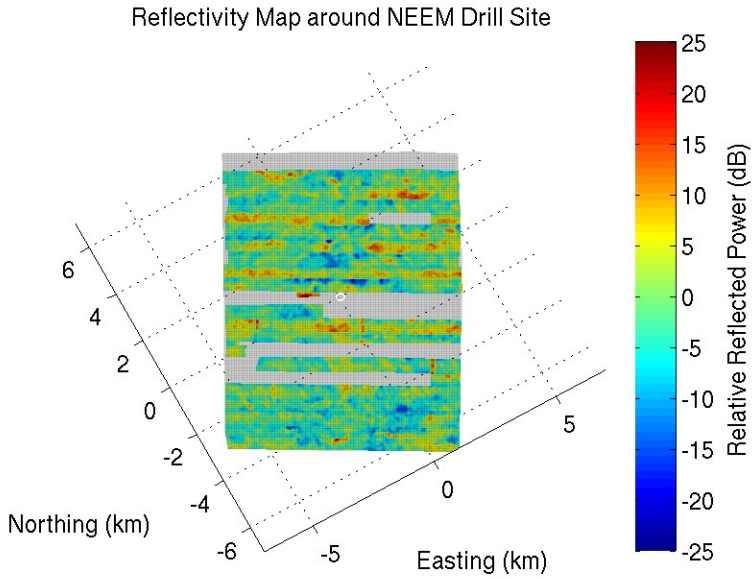

Figure 4.69: Reflectivity mosaic from northeast looking lines

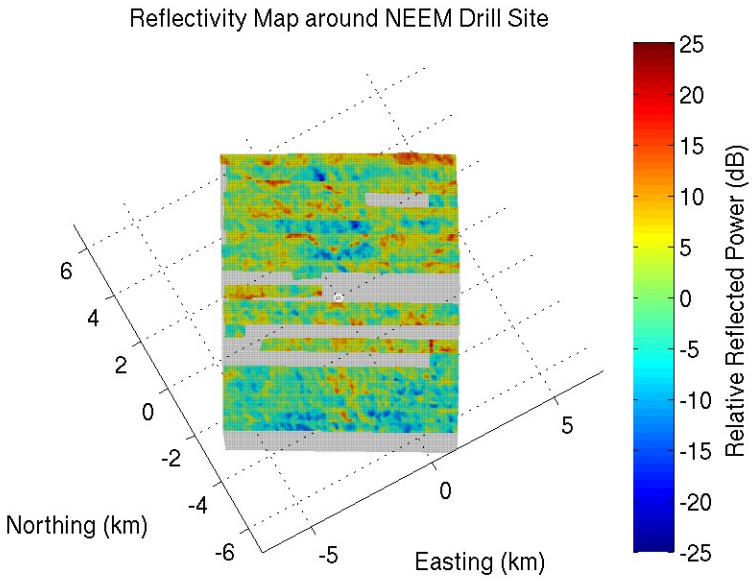

Figure 4.70: Reflectivity mosaic from southwest looking lines

Figures 4.69 is illuminated by the radar from the top of the figure pointed downward and 4.70 is illuminated from the bottom of the figure pointed upward.

After the reflectivity mosaics were created they were draped over the DEM created in the previous section (figure 4.52). These results are shown in figures 4.71 and 4.72.

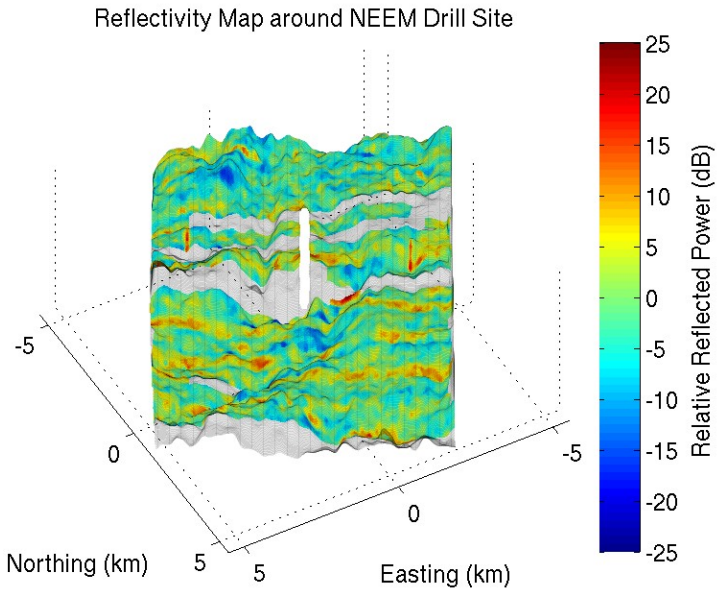

Figure 4.71: Reflectivity mosaic from northeast looking lines overlaying the DEM

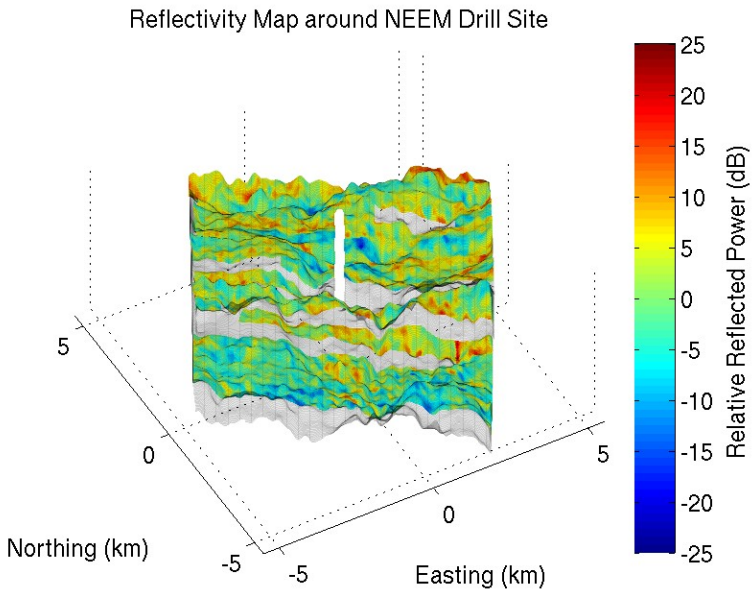

Figure 4.72: Reflectivity from southwest looking lines overlaying the DEM

The perspectives of figures 4.71 and 4.72 are rotated 180 degrees so that the perspective

that is being viewed is the perspective of the radar illumination. The reflected power used for these images was the power after the cross-track mean removal as calculated in section 4.2.13. When necessary the powers were mosaiced using the same cost function as was used for the height estimate. There are a couple bright red spots that are noticeable on these images that could correspond to reflections either from slopes, change in composition, or change in roughness at the bed, further analysis is performed in section 5.3.

5 Scientific Interpretation

There are multiple challenges when trying to determine the conditions at the base of the ice. The three main causes of variations in reflectivity come from slope, roughness, and dielectric contrast. I will remove the variations in slope, and estimate the roughness in order to attempt to see changes in the dielectric contrast.

5.1 Extraction of Slope

One factor that affects the reflected power is the slope of the surface that is being illuminated. To calculate the local slope of the height estimates, the vector normal to each imaged pixel was calculated. The angle of the normal vector with respect to nadir was calculated thus providing the local slope. The local slope was then draped over the InSAR DEM (figure 4.52) An image of the results can be seen in figure 5.1.

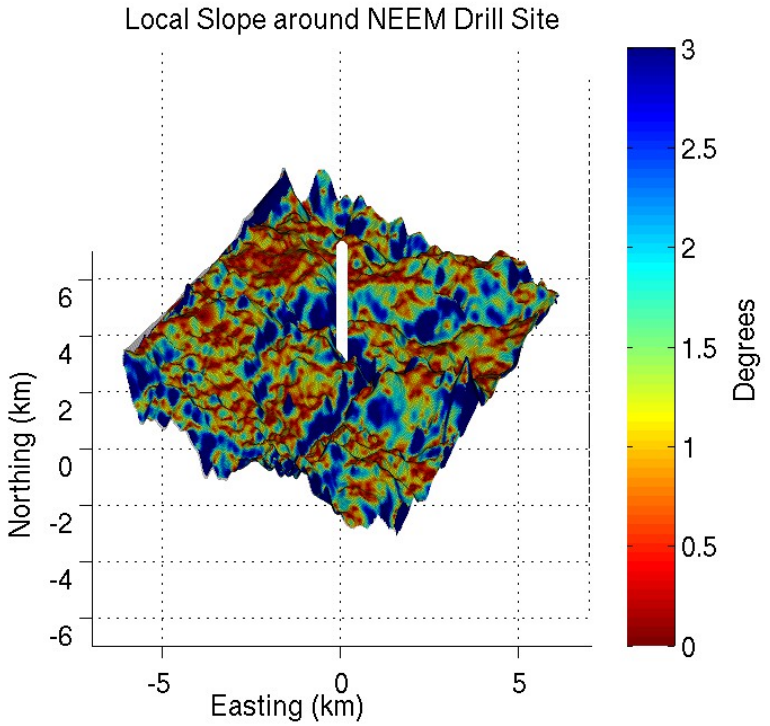

Figure 5.1: Local slope from InSAR DEM

5.2 Extraction of roughness

The slope is important but to understand how the slope affects the reflected power we need an estimate of the roughness. To model the backscatter the physical optics model [Ulaby, Morre, and Fung 1982] was used as this has been use previously at 150 MHz [Allen et al. 1997] to analyze data from ice depth sounding radar. This model assumes:

$\sigma_c^r = 0$

$l > 1.6\lambda$

$l^2 > 2.76\, m\lambda$

$\sigma > 0.25 m$

where σ_c^r is the coherent scattering component, l is the correlation length, λ is the wavelength, and m is the standard deviation of the surface height.

This may not be the optimal model but for a first pass this will be acceptable. The physical optics model simplified to the case of monostatic backscattering with like transmit and receive polarization is:

$$\sigma^0(\theta) = \frac{|R(0)|^2 \exp^{-\left(\frac{\tan^2\theta}{2m^2}\right)}}{2m^2\cos^4\theta} \tag{16}$$

where $|R(0)|^2$ is the Fresnel reflection coefficient at normal incidence and θ is the incidence angle.

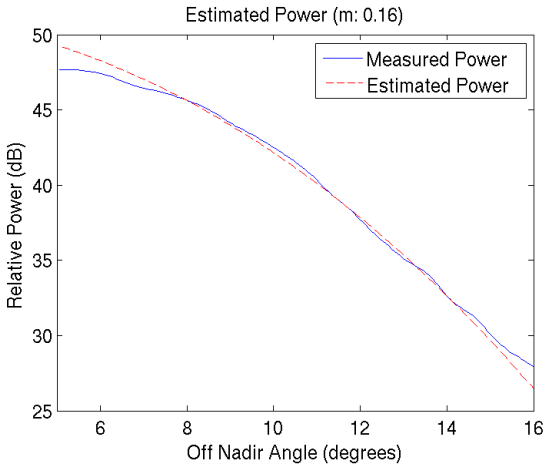

Figure 5.2: Estimated and measured power from August 7th -15° looks

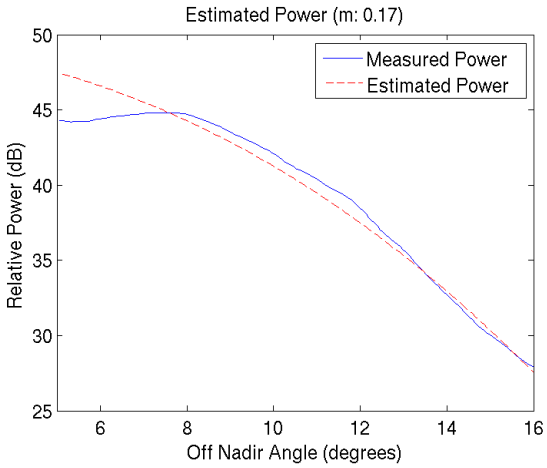

Figure 5.3: Estimated and measured power from August 7th +15° degree looks

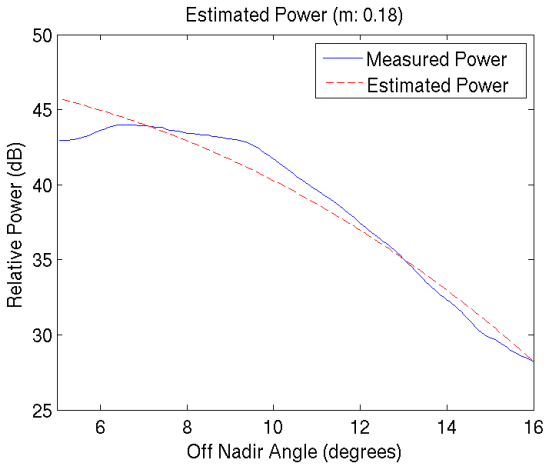

Figure 5.4: Estimated and measured power from August 9th -15° looks

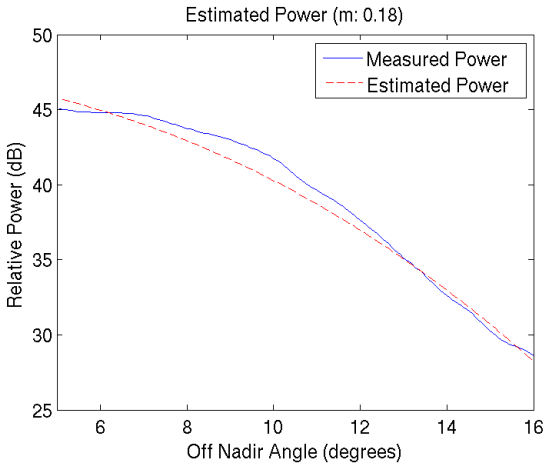

Figure 5.5: Estimated and measured power from August 9th +15° looks

The average power over one day's data provides an average roughness, however what might be more interesting is if there is an area with higher roughness so an average was done of the reflected power over 1-km sections of data for both NE looking and the SW looking reflectivity.

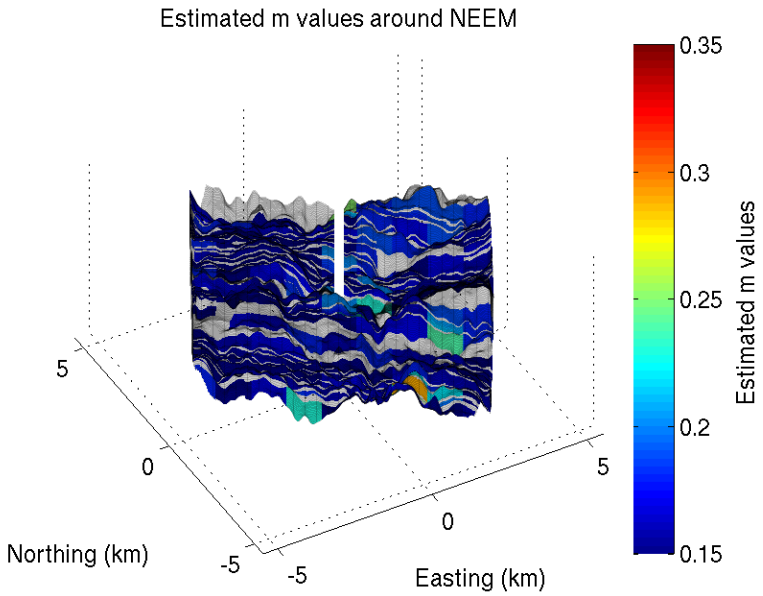

Figure 5.6: Estimated surface height standard deviation from NE reflectivity measurements

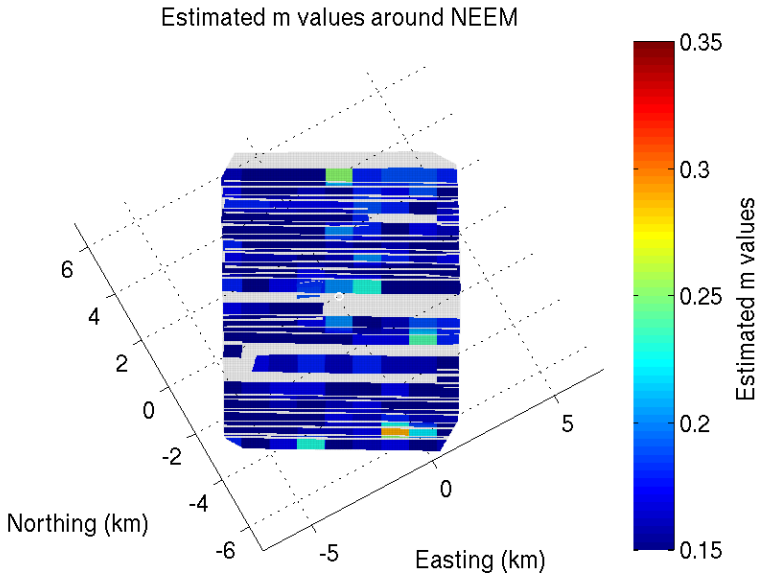

Figure 5.7: Estimated surface height standard deviation from NE reflectivity measurements (bird's eye view)

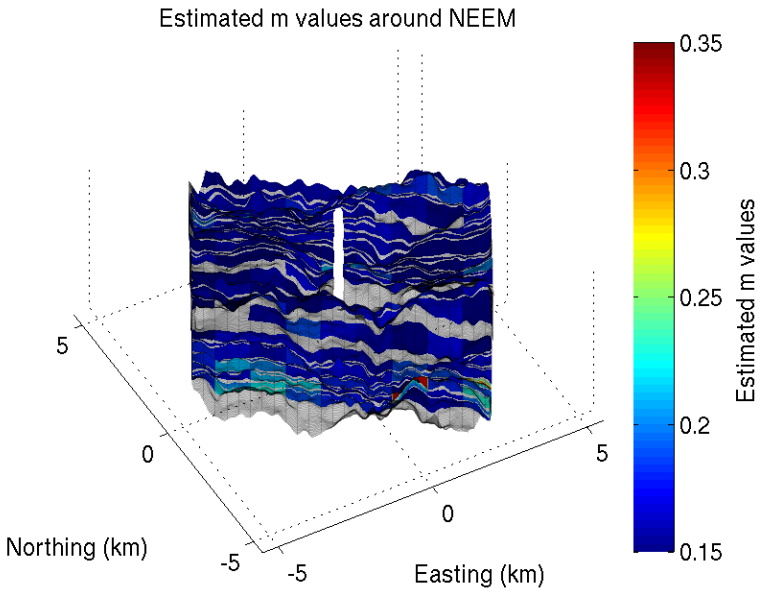

Figure 5.8: Estimated surface height standard deviation from SW reflectivity measurements

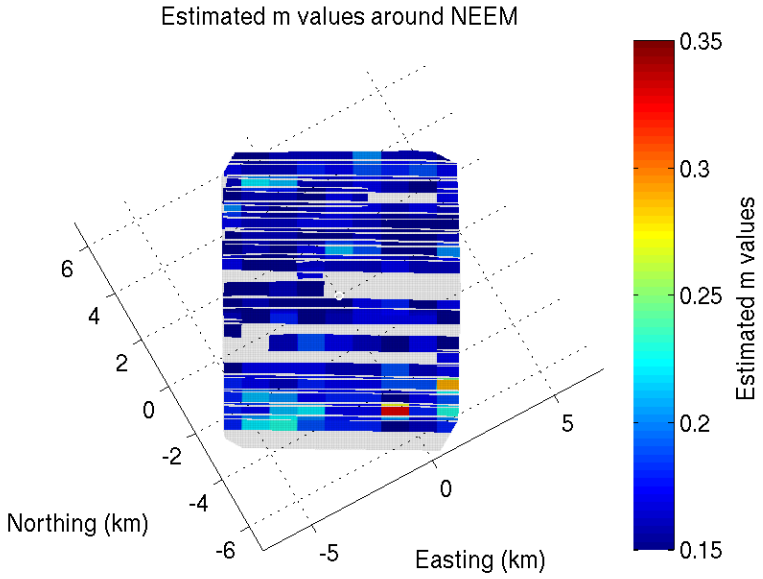

Figure 5.9: Estimated surface height standard deviation from SW reflectivity measurements (bird's eye view)

However with the exception of a few different places the roughness typically varies from

0.15 to 0.24 with an average over all the data of 0.19.

5.3 Estimating Reflectivity

With the local slope, and a way to estimate roughness we can create an estimated reflectivity map. To do this line 2's measured reflectivity was compared with an estimated reflectivity based off the estimated surface height standard deviation for that line (m = 0.16) and the angle to the target The angle to the target was corrected for the local slope by taking the dot product between the vector normal to the surface the normal vector formed by the transmit location and angle to the target.

$$\theta = \cos^{-1}(a \cdot b) \tag{17}$$

where θ is the angle between vectors a and b; a is a unit vector normal to the surface, and b is a unit vector representing the transmitter look vector.

Figures 5.10 and 5.11 show the measured and estimated reflectivities respectively.

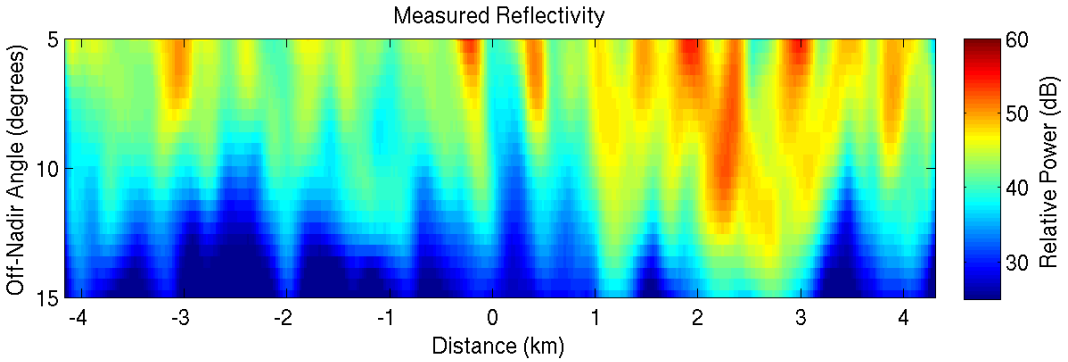

Figure 5.10: Reflected power from line 2

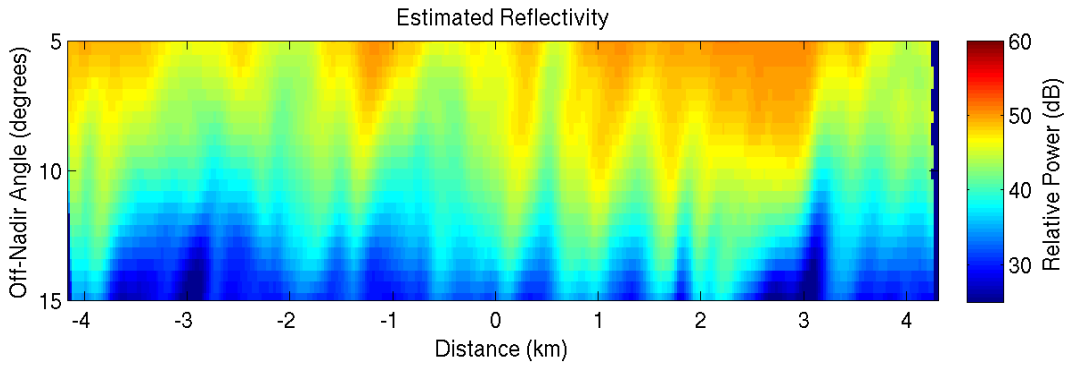

Figure 5.11: Estimated reflected power based using the physical optics model

There are similar general trends in the measured versus estimated reflectivity. However there is some skewing of the reflectivity, possibly caused by either misprojection of the data or inaccurate slopes. The differences between the two reflectivity maps can be attributed to three main causes:

1) Change in basal dielectric contrast over that area possibly due to frozen versus wet bed
2) Violations of physical optics model assumptions
3) Inaccurate slope data

Although there may be some promise there are still some issues to overcome to determine the best way to predict the dielectric contrast of the ice bottom.

6 Conclusions and Future Work

6.1 Conclusions

This work has shown that it not only is possible to perform InSAR through the ice but that the results look promising for extraction of scientific information. A 25-m by 25-m horizontal resolution 3-D basal DEM was created for a 10-km by 10-km grid around the NEEM drill site. Various sources of errors were removed including an amplitude varying interference tone. The InSAR measurements were verified and the errors were shown to be in line with the theoretical values. The RMS basal height error between lines was on the order of a 5-6 meters. These errors are comparable to a worst case (with 6 dB SNR) calculated accuracy of 18 m and a best case (with 30 dB SNR) of 3 meters. This DEM satisfies the basal topography requirements from the science community.

Reflectivity images from both the NE and SW looking lines were created and overlain on the basal DEM. This reflectivity mosaic showed varying received power across the DEM, with several high and low reflected areas. While local slope accounts for much of the reflectivity changes, insight regarding basal roughness and dielectric contrast may be revealed through analysis of these reflectivities.

A method to extract science information from the basal DEM and reflectivity mosaics was proposed using the physical optics model. This provided a fairly consistent roughness estimate across the surveyed grid, with a couple areas of higher roughness left for analysis in future work. Additionally a simulated return was created based off the estimated roughness and

the local slope in the area that showed general agreement with the actual return providing promise that changes in the dielectric contrast (and hence wet versus dry) may be able to be determined. This analysis partially fulfills the science community's requirement for mapping basal conditions.

6.2 Future Work

InSAR provides a very powerful technique to create 3D images of basal terrain. However, there are some challenges associated with correctly geolocating the data. Correctly understanding the effects of the antenna coupling from the air into the firn is very important, as well as the antenna beam through the firn into the ice. An extension of this work is to perform InSAR from an airborne platform. Challenges to extend this work to an airborne platform include correcting motion errors and taking into account the refraction at the air-ice boundary. From a height above the surface, the swath of an airborne platform could be larger, (approximately equal to the height of the platform, i.e. 500 m height above the surface provides 500 m of additional swath width, see figure 6.1) however this may require more power to get adequate SNR. Another aspect to consider is the amount of overlap between the swaths. Overlapping swaths requires no more than half the swath width spacing between lines. This is not required but it makes verification easier. It is also important to have crossing lines for verification purposes.

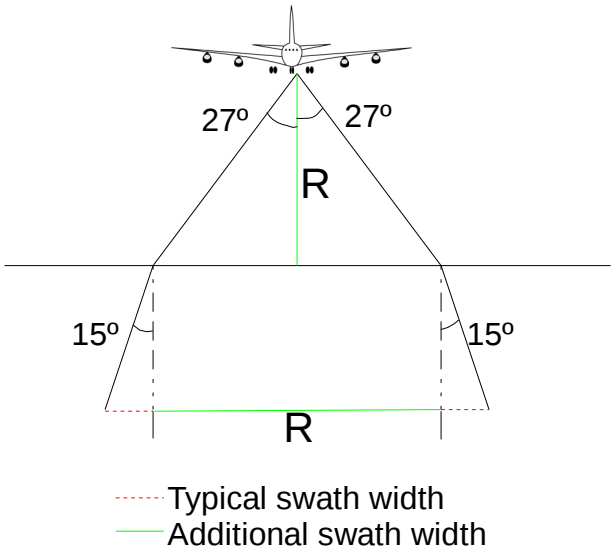

Figure 6.1: Geometry for airborne platform

Further examination of the benefits and shortcomings of InSAR in comparison with tomography need to be looked at as it relates to 3-D basal ice sheet imaging. InSAR requires a continuous surface which is usually a good assumption but if the SNR were to drop to a level that would cause significant phase errors or completely lose the surface, then the unwrapping of phase would fail. This is what limited the InSAR swath to around 900 m off nadir. To address the issue of a surface with varying SNR tomography using MUSIC can be used. While MUSIC requires an adequate SNR to work, this is similar to requirements on InSAR. From this work it was shown that InSAR required at least 6 dB SNR to have accurate phase information, the MUSIC requirements are similar. However tomography does not assume a continuous surface, therefore it could be used to map broken internal layers or other broken surfaces. To perform InSAR processing it was required that the beam be steered either to the left or right to get adequate isolation between the two returns. Since isolation between left and right can not be

achieved close to nadir, with typical beam forming, InSAR can not be performed within a few degrees of nadir. MUSIC can be used to map a swath all the way through and including the nadir return as it has no spatial requirement for left/right isolation. On the other hand while performing InSAR it is easy to extract the reflectivity information from the data as it is required for InSAR image generation. The MUSIC process does not preserve reflectivity values and therefore separate processing must be done to generate reflectivity values for MUSIC. Both InSAR and MUSIC require a linear antenna array on receive, but InSAR requires 2 transmitters to be ping-ponged to create a spatial baseline during a single pass, while this can benefit MUSIC, it is not a requirement.

There is still more to be done in the scientific interpretation of the data. The assumptions for the physical optics model need to be either confirmed or a different model should be used. More can be done to try to tease apart the effects of local slope, roughness, and dielectric contrast, by possibly modifying the filters over the DEM to determine how much of the reflectivity variations are caused specifically by the local slope, in addition to the refined roughness models. In this work we assumed that the ice attenuation was constant over the area of interest, this should either be confirmed or variations should be taken into account. Some areas of increased roughness were seen in figures 5.6 through 5.9, these should be examined in more detail to determine what was the cause of this increased estimated roughness.

7 References

Allen, C., Gandhi, M., Gogineni, P., Jezek, K., “Feasibility Study for Mapping the Polar Ice Bottom Topography using Interferometric Synthetic-Aperture Radar Techniques.” RSL Technical Report 11680-1. (1997).

“Climate Change and Water.” IPCC Fourth Assessment Report. IPCC technical Paper VI. 2007.

CSARP Overiew Document. “GOAP Document.” https://svn.cresis.ku.edu/listing.php?repname=GOAP&path=%2FDocuments%2F#_Documents_. (2007).

Dall, J., Skou, N., Kusk, A., Kristensen, S.S., Krozer, V., “P-sounder: An Airborne P-band Ice Sounding Radar.” *IEEE Geoscience and Remote Sensing Symposium*. (2007), pp. 4225-4228.

Forster, R., Jezek, K., Hong, G., Gray, A., Matter, K., “Analysis of glacier flow dynamics from preliminary RADARSAT InSAR data of the Antarctic Mapping Mission” *IEEE Geoscience and Remote Sensing Symposium Proceedings*. **4**. (1998), pp. 2225-2227.

Graham, L. C., “Synthetic Interferometric Radar for Topographic Mapping.” *Proceedings of IEEE*, **62**, (June 1974), pp. 763-768.

Hagberg, J.O., Ulander, L.M.H., Askne, J., “Repeat-Pass SAR Interferometry Over Forested Terrain.” *IEEE Transactions on Geoscience and Remote Sensing*. **33**. (March 1995), pp. 331-341.

Harris, F.J. “One the Use of Windows for Harmonic Analysis with the Discrete Fourier Transform.” Proceedings of the *IEEE*. **66**. (January 1978), pp. 51- 83.

Heliere, F., Chung-Chi, L., Corr, H., Vaughan, D., “Radio Echo Sounding of Pine Island Glacier, West Antarctica: Aperture Synthesis Processing and Analysis of Feasibility From Space.” *IEEE Transactions of Geoscience and Remote Sensing.* **45**. (August 2007), pp. 2576-2582.

Just, D., Bamler, R., “Phase Statistics of Interferograms with Applications to Synthetic Aperture Radar.” *Appl. Opt.* **33**. (1994), pp. 4361–8.

Le Gall, A., Ciarletti, V., Berthelier, J.-J., Reineix, A., Guiffaut, C., Ney, R., Dolon, F., Bonaime, S., “An Imaging HF GPR Using Stationary Antennas: Experimental Validation Over the Antarctic Ice Sheet.” *IEEE Transactions on Geoscience and Remote Sensing.* **46**. (December 2008), pp. 3975-3986.

Jezek, K., Rodriguez, E., Gogineni, P., Freeman, A., Curlander, J., Wu, X., Allen, C., Kanagaratnam, P., Sonntag, J., Krabill, W., ”Glaciers and Ice Sheets Mapping Orbiter.” *J. Geophys. Res.* **111.** (2006), pp. 1-9.

Jezek, K., Rodriguez, E., Gogineni, P., Freeman, A., Curlander, J., Wu, X., Allen, C., Krabill,

W., Sonntag, J. (2006). *Glaciers and Ice Sheets Mapping Orbiter Concept. European Conference on Synthetic Aperture Radar (EUSAR)*, Dresden, Germany, May 2006.

Li, F., and Goldstein, R. M., "Studies of Multibaseline Spaceborne Interferometric Synthetic Aperture Radars." *IEEE Transactions on Geoscience and Remote Sensing*. **28**. (1990), pp. 88-97.

Lohoefener. A., "Design and Development of a Multi-Channel Radar Depth Sounder." Master's Thesis, Department of Electrical Engineering and Computer Science, University of Kansas, November 2006.

Paden, J., Akins, T., Dunson, D., Allen, C., Gogineni, P., "Ice-sheet bed 3-D tomography." *Journal of Glaciology*. **56**. (2010), pp. 3-10.

Paden, J., "Synthetic Aperture Radar for Imaging the Basal Conditions of the Polar Ice Sheets." Ph.D. Dissertation, Department of Electrical Engineering and Computer Science, University of Kansas, August 2006.

Ronnau, J., Haimov, S., Gogineni, S.P., "The Effect of Signal-toNoise Ratio on Phase Measurements with Polarimetric Radars." *Remote Sensing Reviews*. **9**. (1994), pp. 27-37.

Rodriguez, E., Martin, J.M. "Theory and Design of Interferometric Synthetic Aperture Radars." *IEEE Proc*. **139**. (1992), pp. 147-159.

Treuhaft, R., Moghaddam, M., van Zyl, J., Sarabandi, K., "Estimating Vegetation and Surface Topographic Parameters From Multibaseline Radar Interferometry." *IGARSS '96 International Geoscience and Remote Sensing Symposium*, Lincoln, NE, (1996), pp. 978-980.

Ulaby, F.T., Moore, R.K., Fung, A.K., "Microwave Remote Sensing: Active and Passive." *Addison-Wesly Publishing Company*, **II**, (1982), pp. 936.

Van der Veen, C.J. and ISMASS Members., "A need for more realistic ice-sheet models". Cambridge, International Council for Science/Scott Polar Research Institute. Scientific Committee on Antarctic Research. (2007), SCAR Report 30.

Weber Hoen, E., Zebker, H., "Topography-driven Variations in Backscatter Strength and Depth Observed Over the Greenland Ice Sheet with InSAR." *IEEE Geoscience and Remote Sensing Symposium Proceedings*. **2**. (2000), pp. 470-472.

Yamanokuchi, T., Doi, K., Shibuya, K., "Comparison of Antarctic Ice Sheet Elevation Between ICESat GLAS and InSAR DEM." *IEEE Geoscience and Remote Sensing Symposium.* (2006), pp. 2712-2715.

Yong, P., Zengyuan, L., Guoqing, S., Erxue, C., Zuejian, C., "Comparision of Tree Height Estimations from C and L-band InSAR data." *IEEE Geoscience and Remote Sensing Symposium Proceedings.* **4**. (July 21-25 2003), pp. 2586-2588.

Zebker, H.A., Goldstein, R. M., "Topographic mappping from interferometric SAR

observations." *Journal of Geophysical Research*, **91** (1986), pp. 4993-4999.

Zebker, H.A., Villasenor, J. "Decorrelation in Interferometric Radar Echoes." *IEEE Trans. Geosci. Remote Sns.* **30**. (1992), pp. 950-9.

Zhong, L., Kwoun, Oh-ig., "Radarsat-1 and ERS InSAR Analysis Over Southeastern Coastal Louisiana: Implications for Mapping Water-Level Changes Beneath Swamp Forests." *IEEE Transactions on Geoscience and Remote Sensing*. **46**. (August 2008), pp. 2167-2184.